Three-Dimensional Morphology of Polymer Nanocomposites Characterized by Electron Tomography

Ya-Peng Yu

Thesis submitted to the faculty of the Virginia Polytechnic Institute and State University in partial fulfillment of the requirements for the degree of

Master of Science in

Materials Science and Engineering

Mitsuhiro Murayama

William T. Reynolds

Sean G. Corcoran

June 15, 2016

Blacksburg, Virginia

Keywords: electron tomography, three-dimensional morphology, polymer nanocomposites

Three-Dimensional Morphology of Polymer Nanocomposites Characterized by Electron Tomography

Ya-Peng Yu

Abstract

Electron tomography is an invaluable technique with the capability of carrying out thorough 3D structural, chemical and morphological characterization of materials at nanometer scale. Tilting range, increment and reconstruction algorithms are three of the main factors affecting the quality of tomograms. An anisotropic degradation can be observed with restricted tilting range and increment. Therefore, this study was carried out to investigate the accuracy of the reconstruction results of MgO (cube-shape) generated by FBP, SART and SIRT tomographic algorithms under various reconstruction conditions, i.e. tilting range and increment. Examining the experimental data with known morphology permits quantitative determination of the accuracy of the reconstruction results by measuring the distortion of the cube in all directions. Moreover, distortion measurements in all directions reveal the relationship between level of distortion and the alpha tilt angle.

Acknowledgements

I would like to express my deepest gratitude to my advisor Dr. Mitsuhiro Murayama and Dr. W.T. Reynolds Jr, for their full support, guidance, understanding and encouragement throughout my study and research.

I would also like to thank SEM specialist, Stephen McCartney, for the SEM and microtome training; TEM specialist, Christopher Winkler, for the TEM training and my friend, Chun-Hsien Wu, for the experimental advice.

Finally, I would like to thank my family for their unconditional love and support. I would not have been able to complete this thesis without their continuous love and encouragement.

Table of Contents

List of Figures

Chapter 1 Introduction

Chapter 2 3D Reconstruction Procedure for MgO Tomograms

Chapter 3 Qualitative and Quantitative Comparisons of MgO Tomograms

Chapter 4 Case Study

List of Tables

Chapter 2 3D Reconstruction Procedure for MgO tomograms

Chapter 3 Qualitative and Quantitative Comparison of MgO Tomograms

Chapter 4 Case Study

Chapter 1

Introduction

Development of nanomaterials has become a prevalent field in science. With the increasing complexity of materials, interpretations provided based on two-dimensional (2D) characterization results are limited. For example, various orientation dependent measurements including particle size, elemental distribution and inter-particle spacing are not always accurate because of the projection effect, meaning that distances measured from projected images can be foreshortened or the features can be overlapped in the projection direction and cause the projected length and projected spacing to deviate from the true values (Figure 1.1).[1] Therefore having the ability to perform quantitative three-dimensional (3D) analysis becomes crucial, especially for analyzing nanomaterials without prior knowledge of the structure. Electron tomography is an invaluable technique with the capability of carrying out thorough 3D structural, chemical and morphological characterization of materials at nanometer scale. Studies have proven electron tomography robust to provide informative measurements. For instance, the preferential location of nitrogen was successfully revealed from nitrogen doped CNTs[2]; accessibility of mesopores and pore size distribution were determined from the reconstructed volume of zeolite Y crystals;[3] 3D morphology of a clay/polymer nanocomposite was studied by electron tomography to reveal the shape and orientation of each clay layer[4], etc.

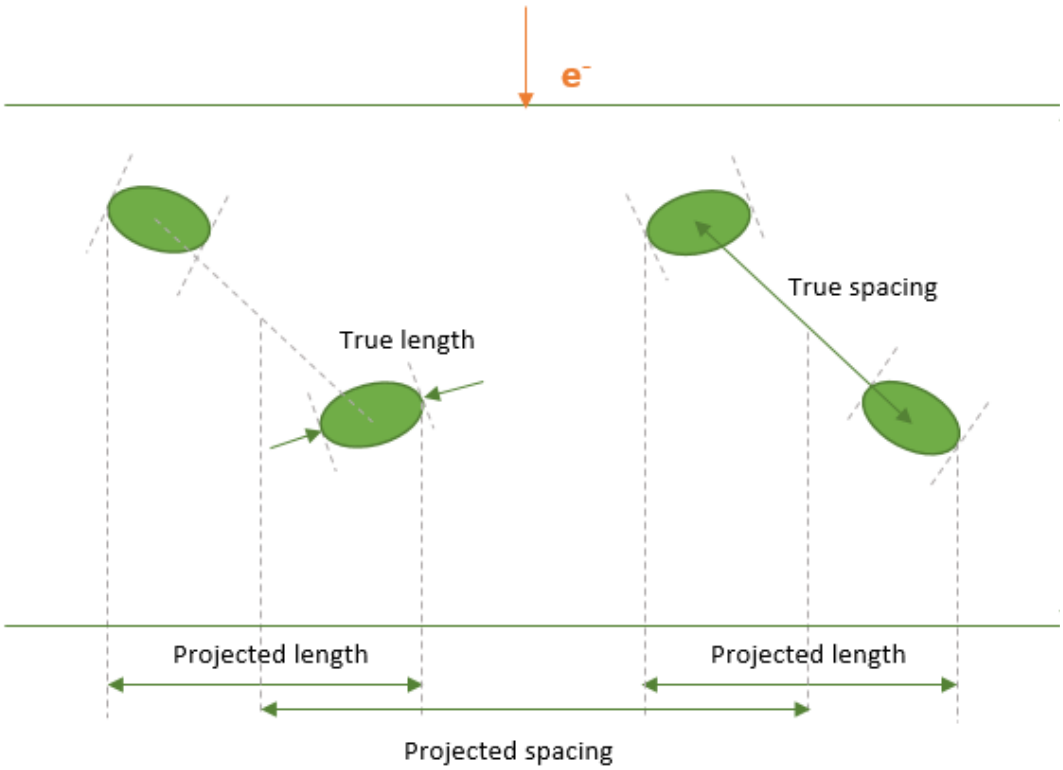

Figure 1.1. Iillustration of projection effect on TEM image. Projected length and projected spacing are overestimated in this case (after Monseque et al. reference[1])

In general, real-space representations of morphologies in multi-directions can be revealed from a series of projection images at different views, which are subsequently aligned, reconstructed and visualized using computational methods. The fundamental principle of electron tomography was originally adapted from the Central Section Theorem[5]: the Fourier transform of a 2D projection of a 3D object at a given angle is a central section of the Fourier transform of that object (Figure 1.2). Therefore, the 3D structure of the specimen in real space can be obtained with an inverse Fourier transform of 3D Fourier transform assembled by 2D Fourier transforms of the tilt-series images.[5] In the following sections, each step of electron tomography will be reviewed, along with the challenges and possible solutions.

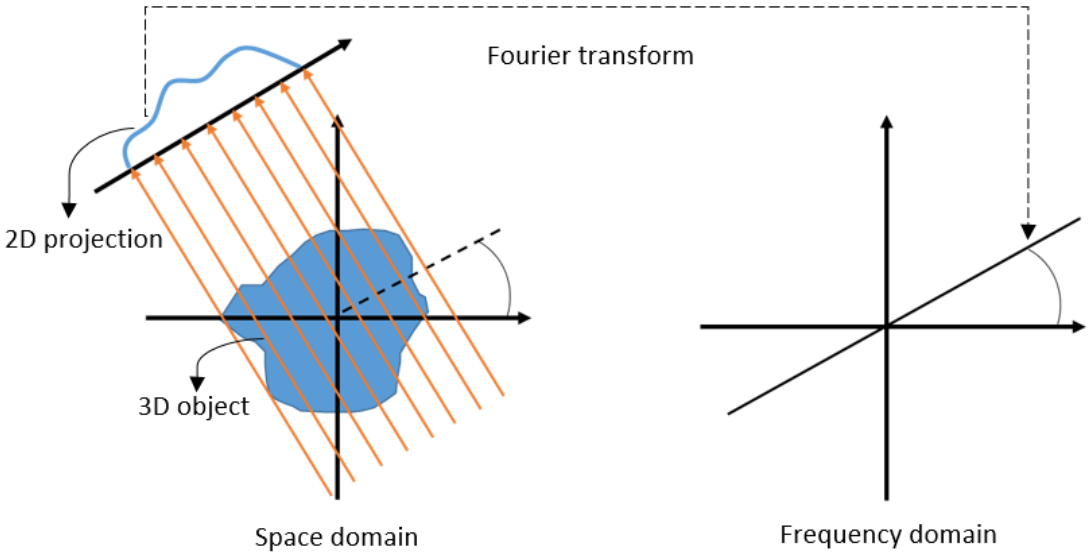

Figure 1.2. Central Section Theorem relates the Fourier transform of a 2D projection to the Fourier transform of the 3D object

Tilt-series image acquisition

In the first step of electron tomography, a series of projection images is recorded by tilting the specimen at different angles with respect to a single axis perpendicular to the electron beam (Figure 1.3); projection images of the specimen collected at different angles are referred as tilt-series images. In an ideal condition, acquisition of tilt-series images should cover the entire tilting range (±90°) with each image fulfills projection requirement, i.e. the intensity of the image is a monotonic function of the physical property to be reconstructed. However, because of the geometry of the microscope and the location of the feature, data collection is limited to tilting angles (from ±35° to mechanical limit around ±80°), leading to a missing wedge of information in Fourier space and artifacts in the reconstructed volume. There is a mechanical limit around ±80° because electron beams travel in the direction perpendicular to the holder and hit the specimen to generate signal in TEM. At high tilting angle, the majority of the electron beams are blocked by the edge of specimen holder, limiting the range of image collection. Resolution along the electron beam direction can be significantly reduced under the effect of missing wedge. To alleviate the missing wedge effect, dual-axis tomography is developed by combing the tilt-series images obtained from two orthogonal tilt axes. With an additional tilt-series dataset, the missing wedge in Fourier space is reduced to a smaller missing pyramid. As the angular coverage is improved, artifacts presented in the reconstructed volume can be substantially reduced.[6,7] A more faithful approach is collecting the projection images with complete tilt over ±90° using a specially modified specimen holder. Kawase et al. achieved an isotropic image resolution of the reconstructed volume by generating a complete set of tilt-series images over angular range of ±90° with a special specimen holder whose edge was cut and shaped to avoid blocking the electron beam.[8]

Electron tomography is based on the assumption that the intensity of projection image is proportional to specimen thickness. Violation of the projection requirement in tilt-series image acquisition step can potentially become an issue; it can be avoided by choosing proper TEM imaging mode. Certain imaging modes are considered to be more suitable for the purpose of satisfying the projection requirement of different types of materials[9]. For example, bright-field (BF) tomography is prevalently used for non-crystalline materials such as biological samples and polymers; it is applied based on the assumption that elastic scattering is dominant; the contrast mechanism is primarily mass-thickness contrast and therefore such imaging condition fulfils the projection requirement for amorphous materials. However, crystalline materials can easily generate diffraction contrast that violates the projection requirement, producing serious artifacts in reconstructed volumes. Diffraction contrast can be greatly reduced by using incoherent scattering in the high-angle annual dark-field scanning TEM (HAADF-STEM) mode, providing the contrast monotonic with atomic number.[10]

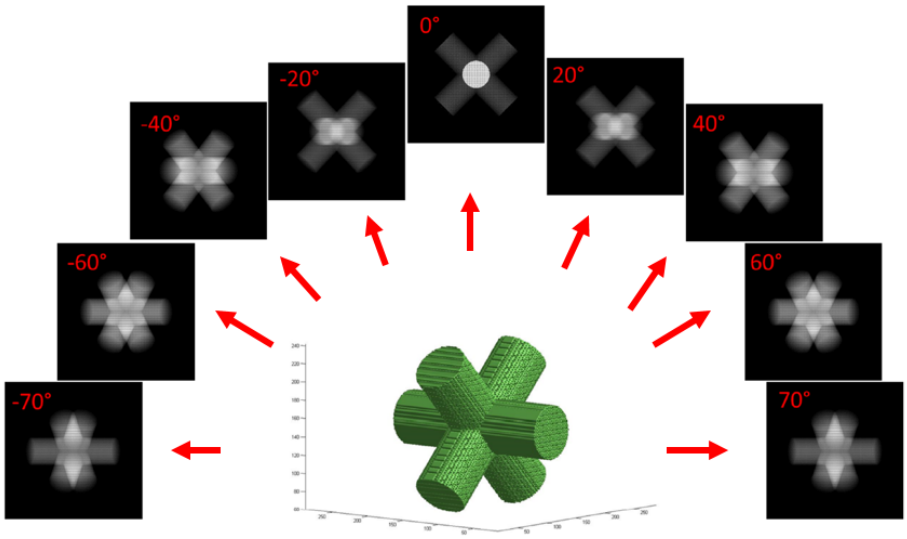

Figure 1.3. tilt-series image acquisition over single tilt axis

Tilt-series image alignment

Position errors of the features caused by mechanical shift during the tilt-series image acquisition step can be severe; though image distortions can be compensated by automated image collection procedure, a more accurate alignment must be performed post-acquisition for high accuracy tomogram. Conventional approaches used to align tilt-series include tracking of fiducial markers and cross-correlation. Fiducial markers with known morphology (typically colloidal gold beads) are dispersed in the specimen and used as reference points for alignment. Coordinates of the fiducial markers are recorded throughout the tilt-series dataset and are further used to implement image alignment by minimizing the alignment error as a function of image shifts,

rotations and other parameters. Alignment based on fiducial markers determines not only spatial movements e.g. relative lateral shift, image rotation, magnification change, and any secondary distortions, but also the tilt axis direction. However, the high contrast of fiducial markers can mask details in the reconstructed volumes. Markerless alignment can be performed by cross-correlation of successive images. For each image, the level of image shift is equal to the cosine of tilting angle in the direction orthogonal to tilt axis. To reduce the cumulative shift error, tilt-series images are spilt into two parts, each using zero-tilt image as the first reference and applying alignment all the way toward the highest tilting angle in both directions. For cross-correlation approach, only lateral shift can be determined, additional techniques are required to determine the tilt axis direction and compensate other distortions.[9,5]

Tomographic reconstruction

As mentioned previously, generating an electron tomography is fundamentally based on the mathematical principles of Central Section Theorem; the 3D structure of the specimen in real space can be obtained with an inverse Fourier transform of 3D Fourier transform assembled by 2D Fourier transforms of the tilt-series images.[5] However, the interpolation in Fourier space is non-trivial; alternatives such as Filtered back-projection (FBP), simultaneous iterative reconstruction technique (SIRT) and simultaneous algebraic reconstruction technique (SART) are applied in practice.

The concept of FBP reconstruction algorithm is essentially equivalent to central section theorem, but working in real space. In the calculation step, projection images are assumed to represent the mass density of the object encountered by imaging rays. By assembling the projection images at different views, the mass of the original structure is revealed at the intersection points of the back-projection rays[5] (Figure 1.4). The reconstructed volume generated by the back projection approach is blurred because of the enhancement of low frequencies and the poor reconstruction of fine spatial details. To properly represent the high frequency information of the reconstructed volume, a high-pass filter is required to alleviate the effect of uneven sampling of spatial frequencies in the ensemble of original projections.[9] FBP has become a standard tomographic reconstruction method owing to its speed of execution; nevertheless, its sensitivity to tilting angle and noise is one disadvantage to be resolved.[5,9,11]

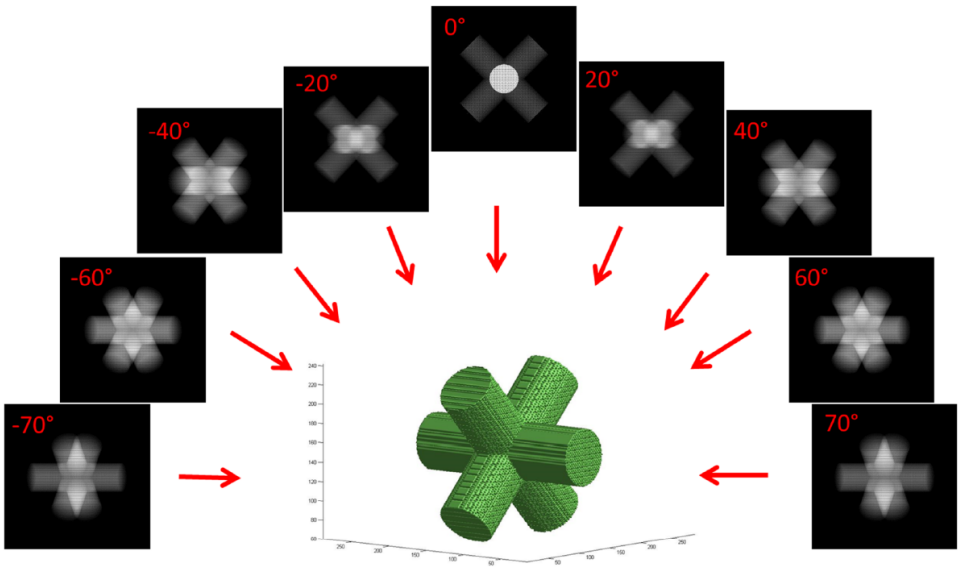

Figure 1.4. Principles of FBP

With the advance of computational power, iterative reconstruction techniques such as SIRT and SART are increasingly adopted. In the calculation step, the projection images are converted into a large system of linear equations and solved simultaneously to generate the reconstruction (Figure 1.5). In every iteration: (1) projections of the current reconstructed volume are computed (2) errors between the original TEM projection images and projections of the current reconstructed volume are calculated (3) reconstructed volume is refined by minimizing the average error (4) repeat to the next iteration. The procedures of iterative algorithms are generally the same, but differ in the way to minimize the average error. As the reconstructed volume are repetitively adjusted in each iteration to best fit the original TEM tilt-series images, it is essentially crucial to accurately align the tilt-series images; otherwise, the minimum average errors could propagate in different directions. Iterative reconstruction algorithm has been widely utilized because of its capability of overcoming the tilting angle and noise issue; however significant artifacts are still present as a result of highly underdetermined system of equations and the discrete dataset, which are inherent in the technique and cannot be resolved.[5,11]

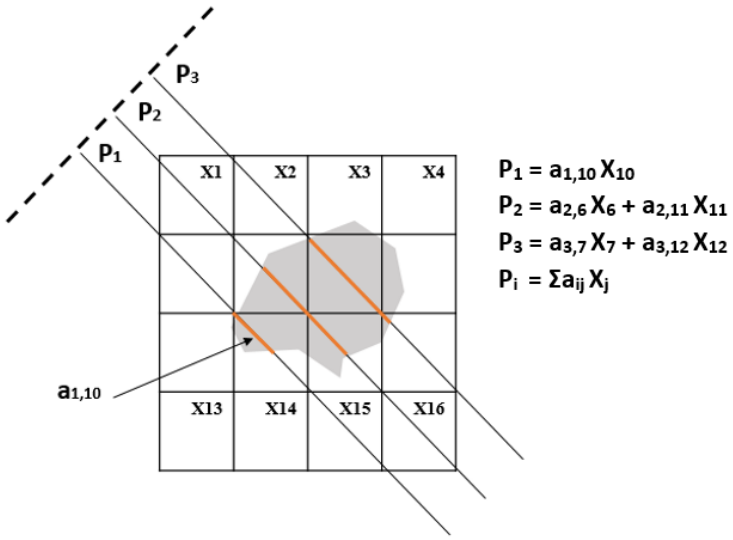

Figure 1.5. system of linear equations used in algebraic reconstruction techniques (after Monseque et al. reference)

Restricted factors of electron tomography

Leary et al.[12] systematically compared the fidelity of tomographic algorithms under various reconstruction conditions, specifically the fidelity of compressed sensing (CS) algorithm, which is a process of signal recovery from under-sampled data; it has proven useful in reconstruction of beam sensitive materials as fewer projection images are required. In Leary's first case study, CS, SIRT and FBP-reconstructed volumes were obtained from the projections of a 2D test phantom consisting of 3 ring-shaped objects. The accuracy of the reconstruction results was determined by intensity histograms of the phantom and tomograms, revealing a much greater quantitative correspondence between the CS-tomogram and the phantom compared to the SIRT and FBP-tomograms. Moreover, from the image intensity line profiles of phantom and tomograms, the distortion in the missing wedge direction visible in the SIRT and FBP intensity profiles was significantly reduced in the case of CS; the intensities of the background and test object were recovered more accurately by CS. The accuracy was also calculated by a normalized ℓ_2-error metric between phantom and tomogram as well as a normalized ℓ_2-difference between re-projections of the reconstructed volume and the original projections. For this ring-shaped test phantom case study, all the fidelity measurements show greater correspondence for CS, and least correspondence for FBP. Further analysis was carried out by Leary to investigate the accuracy of reconstructed volumes obtained from experimental data. In the second case study, CS and SIRT reconstructions were performed using 27, 13 and 9 projection subsets from the full tilt-series of concave iron oxide nanoparticles and cadmium selenide/telluride tetrapods.[12] A normalized ℓ_2-difference between re-projections of the reconstructed volume and the original projections were measured, giving that both the CS and SIRT-tomograms have similar errors with respect to the noisy sonogram.[12]

The effect of missing wedge on distortion and artifact was studied by Saghi et al using needle-shaped biological specimens. For a full tilting range (-90°:1°: +90°) of FBP reconstruction, high fidelity 3D structural information uncorrupted by artifacts was observed. However, reconstructed volume with restricted tilting range of ±60° showed an anisotropic degradation, where horizontal features were partially absent when the missing wedge was simulated in vertical direction, whereas the vertical features were partially absent when the missing wedge was simulated in horizontal direction. By qualitatively comparing the features from cross-sectional slices, the study concludes that missing wedge artifacts can become pronounced when seeking to image objects that have elongated features perpendicular to the tilt axis; features can be partially or completely lost because of important Fourier components lying in the missing wedge region. The study was further carried out to examined the effect of tilt increment. For a dataset with full tilting range and small increment (1° and 2°) the CS and FBP algorithms perform similarly. However, as the increment increased to 4° and 7°, severe artifacts and low signal-to-noise-ratio were found on FBP-tomograms; on the other hand, features in CS-tomograms were less affected by streaking artifacts.[13]

As stated from the literature mentioned previously, data collection is often restricted by the nature of the sample and hardware design. For example, because of the geometry of the microscope and the location of the features, data collection can be limited to a restricted range of tilting angles. For beam sensitive materials such as biological samples and polymers, tilt-series are constrained to larger angular step to minimize the total electron dose. Tilting range, increment and reconstruction algorithms are three of the main factors affecting the quality of tomograms. Therefore, it is worth comparing the accuracy of the tomograms generated by different tomographic algorithms under various reconstruction conditions, i.e. tilting range and increment. In this article, 3D reconstructions were carried out on Magnesium oxide (MgO) using FBP, SIRT and SART algorithms under various tilting range and increment. The advantage of choosing MgO as a reconstructed object is the prior knowledge of its cube-shape. Examining the experimental data of a known shape permits quantitative determination of the accuracy of reconstruction result by measuring the distortion of the cube in all directions. Moreover, distortion measurements in all directions could be very informative; it reveals the relationship between level of distortion and the alpha tilt angle.

Chapter 2

3D Reconstruction Procedure for MgO Tomograms

TEM sample preparation and tilt-series acquisition

TEM specimens of MgO nanoparticles were prepared by collecting smoke containing MgO nanoparticles from burning Mg metal on a TEM grid. HAADF-STEM tomography was performed on an FEI Titan 300 operated at 300 kV with a tomography holder (Fischione model 2020). Tilt-series images were acquired in a semi-automated manner using FEI Xplore3D. A total of 155 projections were taken over an angular range of ±77° with 1° tilt increment. The image size of each tilt-series image was 1024 x 1024 pixels; whereas the reconstruction volume was 512 x 512 x 512 voxels.

Quality of input STEM images

Electron tomography assumes the satisfaction of the projection requirement, i.e. the intensity in the projected image is a monotonic function of the 3D object thickness. As shown in Figure 2.1 (a), a line profile was measured along a cube of MgO to investigate the quality of input STEM images; the intensity plot shown in Figure 2.1 (b) indicated a linear relationship between the intensity and thickness. Image saturation occurred in the region where the intensity peak was cropped off and remained constant at position 160 to 220 nm.

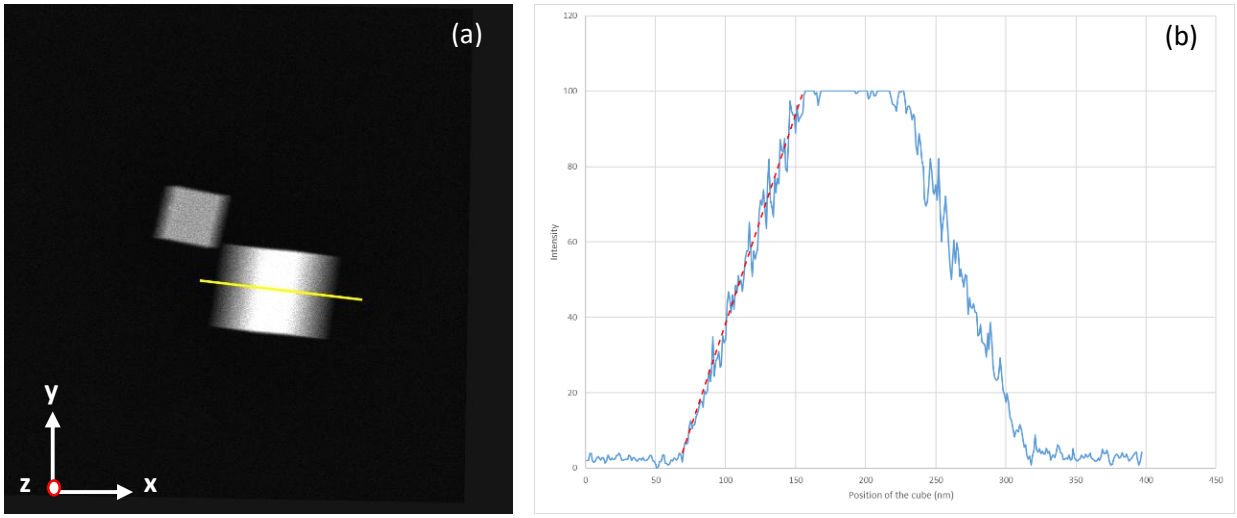

Figure 2.1. (a) HAADF-STEM image of two cube-shaped MgO nanoparticles. The small particle is 207nm on a side, the larger particle is inclined relative to the electron beam (b) the measured image intensity along the line in (a) across the large MgO particle. * y is defined as the rotation axis; z is defined as the beam direction, which is also the missing wedge direction

Reconstruction

Tilt-series images of the MgO particles in Figure 2.1 were aligned by a cross-correlation method using SIF Composer: the alignment was optimized for the large MgO cube. A tomogram of the large MgO cube was reconstructed by FBP, SIRT and SART algorithms using Composer. To inspect how tilting range and increment affect the accuracy of the volume reconstruction, tomograms were reconstructed under the conditions shown in Table 2.1. In experiments A, B, C and D, tilting range varied from 77° to 45° while the increment was held constant; with this setup, effect of titling range can be determined. In experiments A, E, and F, tilting range was held constant while the increments were set at 1°, 5° and 10°, respectively; with this setup, effect of increment on tomograms can be determined. Additional experiments were also performed by (1) varying the tilting range from ±77° to ±45° with a total number of 91 projection images (2) varying the increments from 1° to 10° with tilting range fixed at ± 70°.

Table 2.1. Reconstruction condition of the tomogram

Condition	Tilting range	Increment	Algorithms
A	±77°	1°	FBP, SIRT, SART
B	±65°	1°	FBP, SIRT, SART
C	±55°	1°	FBP, SIRT, SART
D	±45°	1°	FBP, SIRT, SART
E	±77°	5°	FBP, SIRT, SART
F	±77°	10°	FBP, SIRT, SART

Visualization

To investigate the noise, distortion and streaking artifact of the tomograms, several intensity plots were created in both x and y directions (Figure 2.2-2.3). The coordinate system is the same as Figure 2.1, where y is defined as the rotation axis and z is defined as the beam direction. Intensities of 2D STEM image at 0° were measured using Gatan DigitalMicrograph (orange). Original reconstructed volume at 0° was represented as 3D matrix in Matlab; the intensities along x direction were determined by the summation of grayscale in y and z direction; whereas the intensities in y direction were determined by the summation of grayscale in x and z direction (blue), which is effectively a projection image of the reconstruction result (Equation 1).

$$I_x = \sum_{y=1}^{512} \sum_{z=1}^{512} I_{x,y,z} \; ; \; I_y = \sum_{x=1}^{512} \sum_{z=1}^{512} I_{x,y,z} \qquad \text{Equation 1}$$

As shown in Figure 2.2-2.3, deviations between the tomogram and STEM image were observed because the traces of FBP tomogram include the reconstruction artifacts. Deviations along the y direction are minimal for all reconstruction conditions. On the other hand, deviations along the x direction are substantial, which could be contributed by the artifacts from reconstruction process. If a reconstructed volume is accurate, the trace of FBP tomogram will coincide with the STEM image intensity trace for all orientation of the MgO crystal and tomogram. If artifacts and distortions are presented in the reconstructed volume, they can be quantified by the differences between the STEM image trace and the FBP tomogram trace.

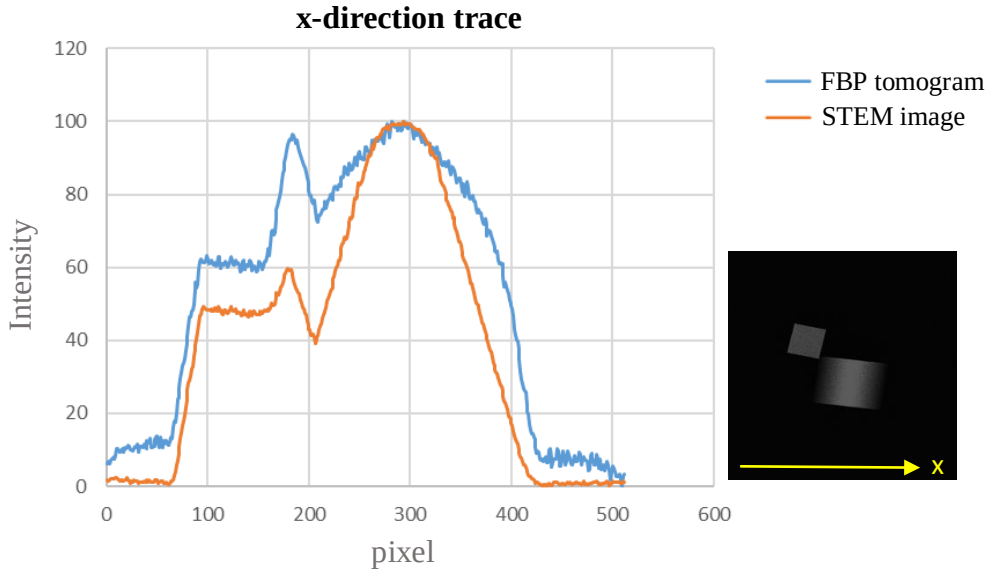

Figure 2.2. Intensity plots of original 2D STEM image (orange) and FBP tomograms reconstructed under condition A (blue) along x direction.

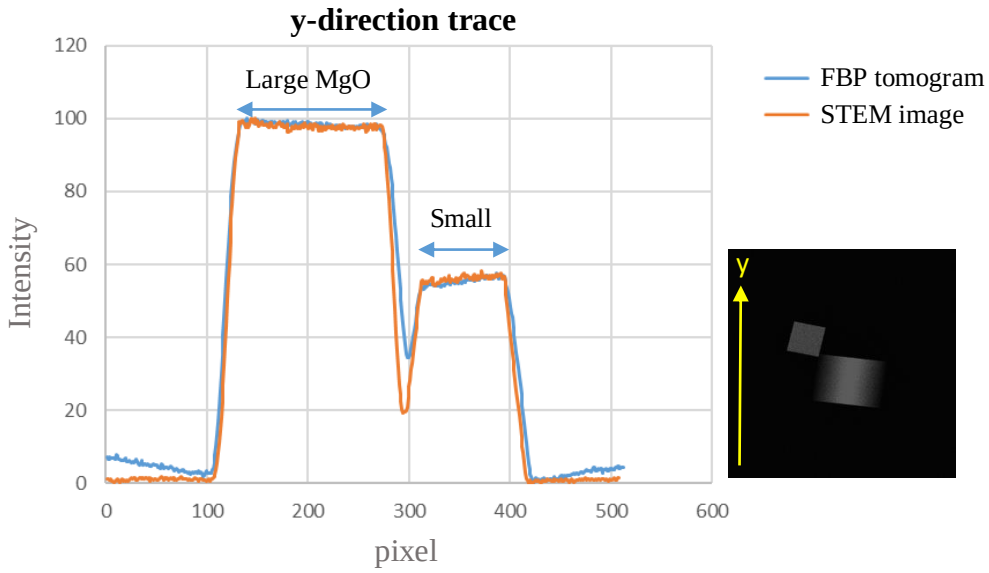

Figure 2.3. Intensity plots of original 2D STEM image (orange) and FBP tomograms reconstructed under condition A (blue) along y direction

Artifact and noise are most significant in the z direction because of the missing wedge effect. The edges of the large MgO cube can hardly be detected from 3D matrix in Matlab without any image filters, therefore a threshold was set to the value at which the large MgO tomograms match the 2D STEM image (xy plane) using SIF Visualizer. Intensities of the filtered tomogram at 0° were then measured by Gatan DigitalMicrograph (gray curves). As shown in Figure 2.4-2.5, gray curves were observed to have better fitting to orange curves in both x and y directions. Furthermore, the edges of the gray curves of the larger MgO coincided with orange curves, meaning that the length of the cube was not altered; the edge of the gray curves of the smaller cube did not properly fit the edge of orange curve (arrow) because image alignment was optimized for the large cube only. Distortions of the small cube were not investigated in this study. Moreover, the periodic intensity oscillations in the gray curves were generated by the support film of the TEM grid. Based on the observations mentioned above, it is appropriate to assume that only the noise and streaking artifact were removed by applying a threshold to the tomogram; the shape of the tomogram was not altered.

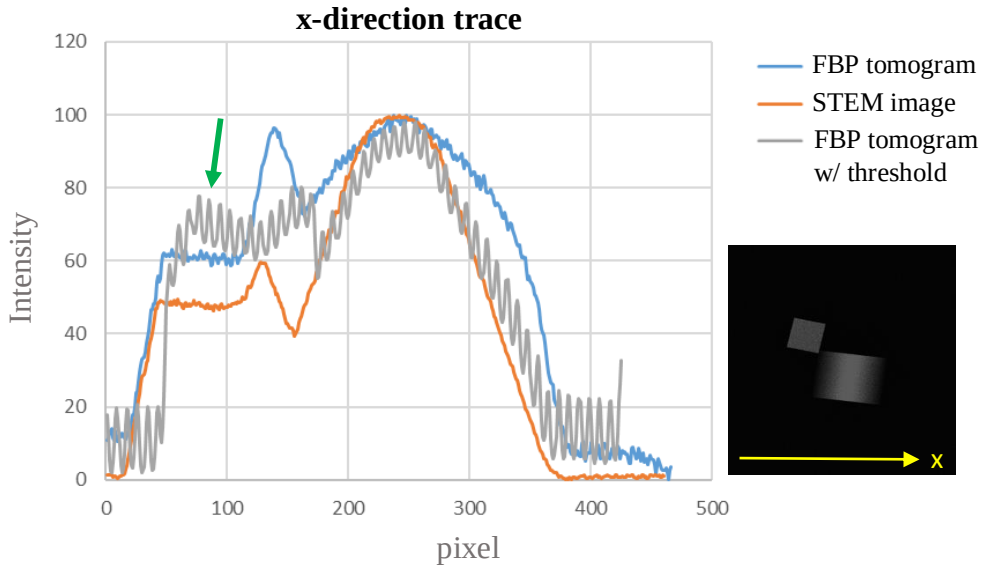

Figure 2.4. Intensity plots of original 2D STEM image (orange), a FBP tomogram without image filters (blue) and a FBP tomogram with the application of threshold value (gray) along x direction.

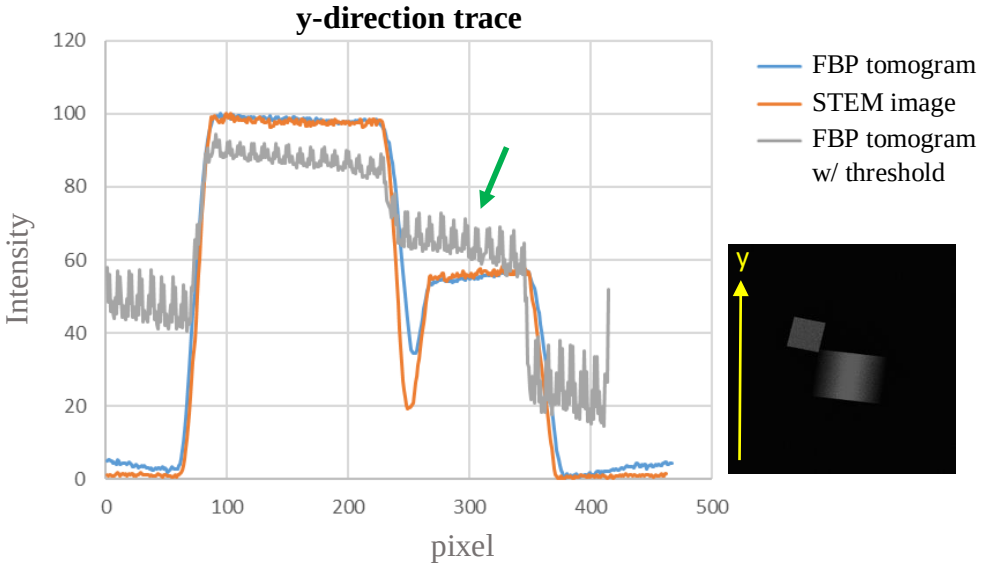

Figure 2.5. Intensity plots of original 2D STEM image (orange), a FBP tomogram without image filters (blue) and a FBP tomogram with the application of threshold value (gray) along y direction.

Simulation model

The advantage of choosing MgO as an object for reconstruction is that the prior knowledge of its cube-shape can be used to validate the dataset. To measure the distortions of the tomograms in all directions, a model was created using autoCAD. The length of the model was determined

using the tilt-series image of α= -50°, where the cube was found to be <001> orientation; angles of the model in x, y and z directions were simulated using Visualizer. The center point of the model was matched to the center point of the tomogram; distortions of the tomogram were determined in a manner shown in Figure 2.6, where the length differences between the tomogram and model were measured over 360°. As shown in Figure 2.6, l is the length of MgO cube; l' is the length of the model. Distortions of the tomogram in horizontal direction can be calculated using equation 2 while distortions of the tomogram at θ degree can be calculated using equation 3.

$$\text{Distortion in horizontal direction} = l - l' \qquad \text{Equation 2}$$

$$\text{Distortion at } \theta \text{ degree} = l\cos\theta - l'\cos\theta \qquad \text{Equation 3}$$

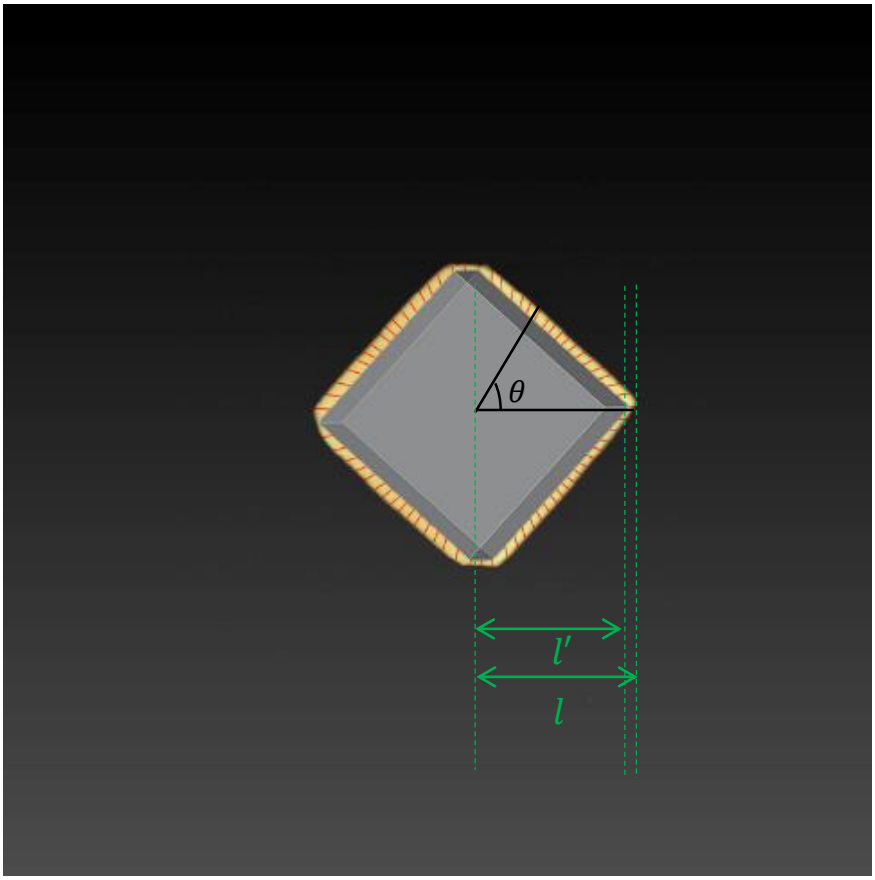

Figure 2.6. Distortion measurements. Yellow area represents the xz plane of the tomogram; gray area represents the xz plane of the model created by autoCAD; red lines represents the distortions of the tomogram, i.e. the length difference between the corresponding points on tomogram and model

Chapter 3

Qualitative and Quantitative Comparisons of MgO Tomograms

The comparison of xz plane of tomograms at different tilting range shown in Table 3.1 qualitatively illustrates the influence of tilting range on reconstructed volumes, confirming the statement from the literature that FBP algorithm is sensitivity to tilting range whereas iterative reconstruction algorithms are robust, particularly for dataset with limited tilting range.[4,5] For FBP algorithm, distortion, streaking artifact and noises become sever as the tilting range becomes smaller, especially in the missing wedge region. Distortion means the stretch of the reconstructed volume (e.g. SIRT, condition D); streaking artifacts are the lines produced in the missing wedge region (e.g. FBP, condition D). For SART algorithms, increases in distortion and artifact are minimal; as for SIRT algorithms, artifact became noticeable when tilting range becomes less than or equal to 55°. Additional experiments were performed by varying the tilting range from ±77° to ±45° with a total number of 91 projection images; all results were found to be similar to the results obtained from experiments A-D. For the results shown in Table 3.1, y is defined as the rotation axis; z is defined as the beam direction, which is also the missing wedge direction. The voids shown in the center of some tomograms are caused by the threshold, which is set to the value that can remove most noise, but remain the shape of the tomograms.

Table 3.1. xz plane of tomograms at different tilting range

	FBP	SART	SIRT
A 77°	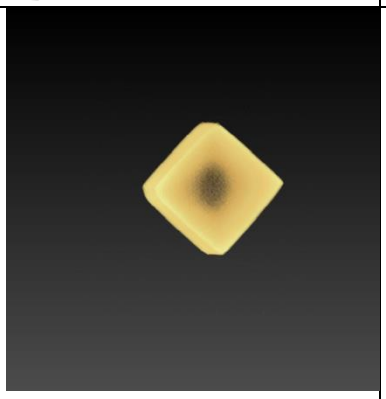	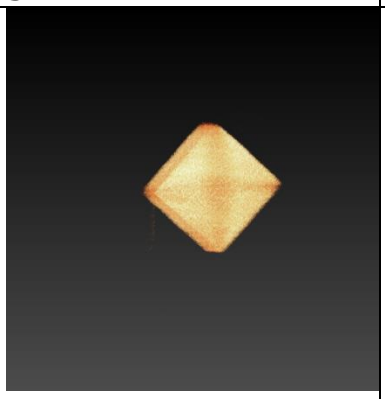	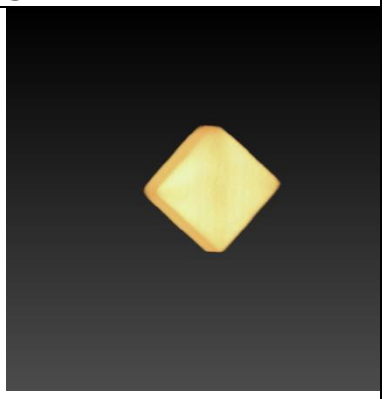
B 65°	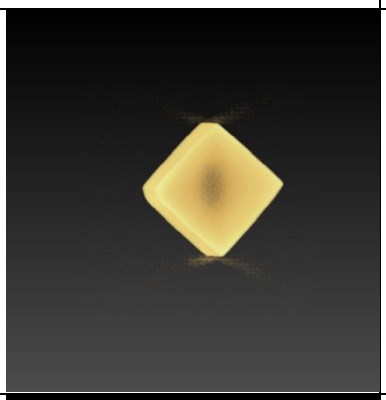	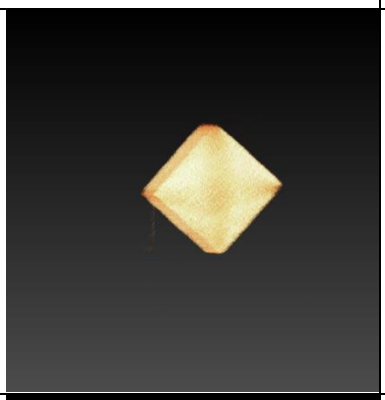	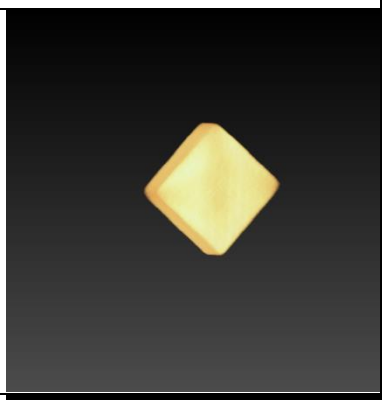
C 55°	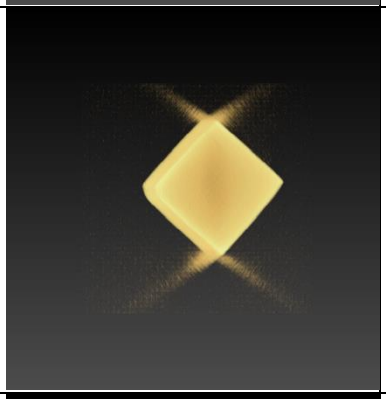	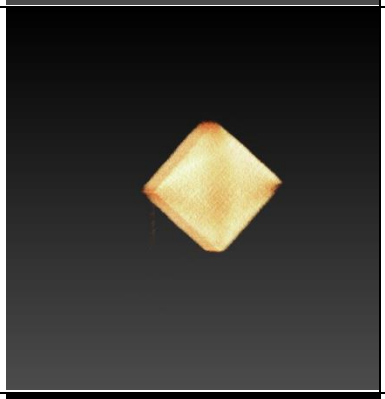	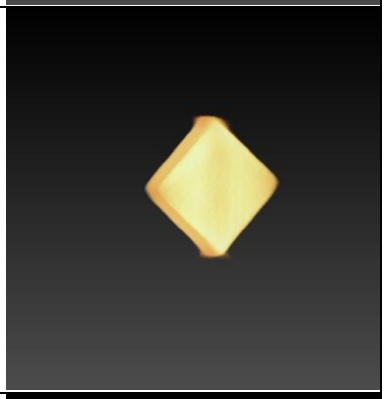
D 45°	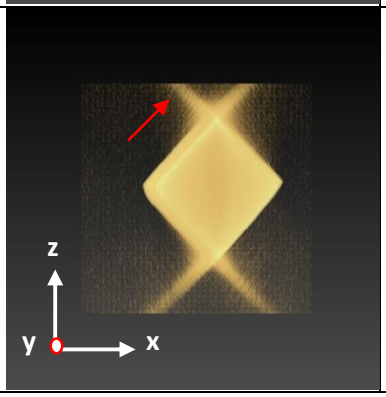		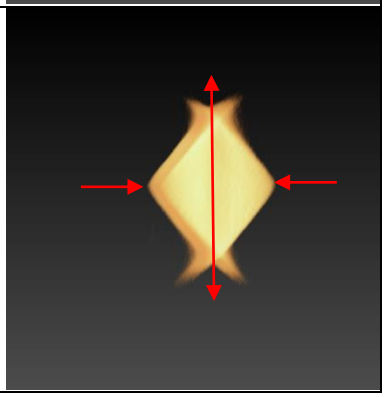

The comparison of xz plane of tomograms with different increment shown in Table 3.2 qualitatively illustrates the influence of tilt-step increment on reconstructed volumes. For FBP algorithm, more noises are generated to the reconstructed volume with larger increment; the shape of reconstructed volumes remain the same regardless of the change in increment. For iterative reconstruction algorithms, SART and SIRT, both the shape of the volume and the level of noise are about the same despite the change in increment. Additional experiments were performed by varying the increments from 1° to 10° with tilting range fixed at ± 70°; all results were found to be similar to the results obtained from experiments A, E and F. For the results shown in Table 3.2, y is defined as the rotation axis; z is defined as the beam direction, which is also the missing wedge direction. The voids shown in the center of some tomograms are caused by the threshold, which is set to the value that can remove most noise, but remain the shape of the tomograms.

Table 3.2. xz plane of tomograms with different increments

	FBP	SART	SIRT
A 1°	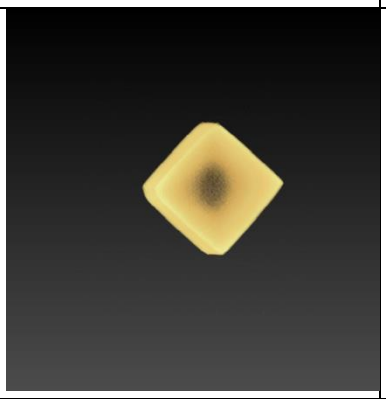	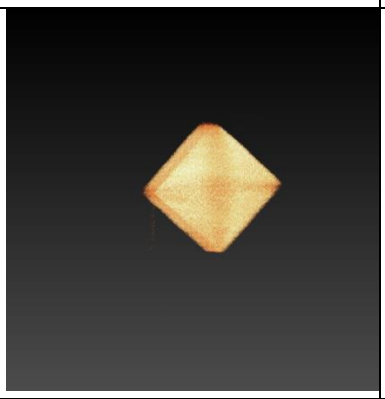	
E 5°	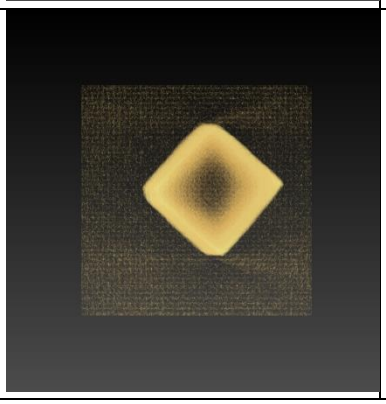	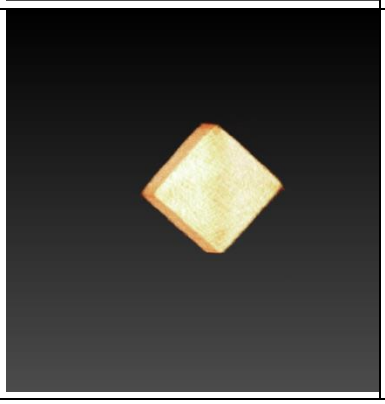	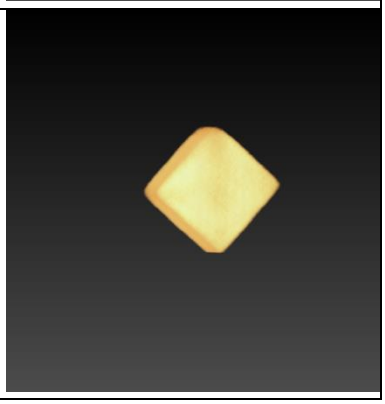

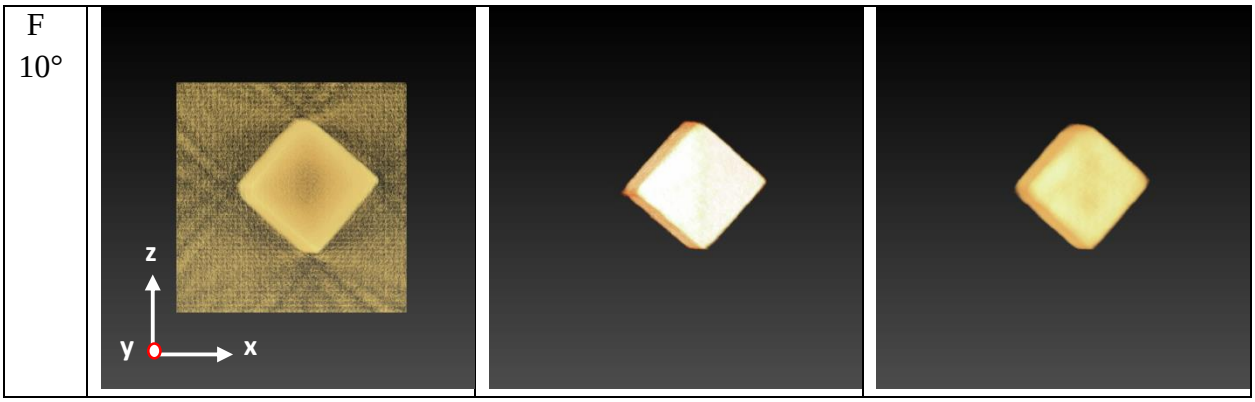

Distortions of tomograms reconstructed under various tilting ranges

For a more precise evaluation, the distortion was quantitatively measured in all directions by overlapping the xz projection of tomograms and CAD model, which can be assumed as the true structure of the reconstructed object. As shown in Figure 3.1. radius of the circle represents the distortion measurement in nm units; the closer the curve to the center, the smaller the distortion, i.e. for a perfect reconstructed volume without any distortions, the measurement will be displayed as a dot at the center point of the circle. The area highlighted in blue represents the missing wedge region.

For tomograms using FBP algorithm at 77° and 65° tilting range, distortion occur in all directions at about 10.7% deviation from the size of the expected volume, except for the cusps at 0°, 90°, 180° and 270°. As the tilting range of FBP tomograms decreases to 55° and 45°, distortions significantly increase in the missing wedge region, which could be as large as 28.6% deviation. For tomograms reconstructed using SART algorithm, distortion measurements are similar for all tilting ranges, which occur in all directions at about 7.9% deviation, except the cusps at 0°, 90°, 180° and 270°. For tomograms reconstructed using SIRT algorithm with ±77° and ±65° tilting range, distortions occur in all direction at about 6.1% and 6.8% deviation respectively, except for the cusps at 0°, 90°, 180° and 270°; distortions become substantial, specifically in missing wedge region, as the tilting range decreases to 55° and 45°, which could be as large as 24.4% deviation. Negative distortions were observed for SIRT algorithms.

Results from Table 3.1 and Figure 3.1 showed that (1) distortions appear in all directions at high tilting range, and start to become severe, specifically in missing wedge region, as the tilting range decreases. (2) Cusps are found within the missing wedge region at high tilting range. (3) distortions can increase substantially as the tilting range decreases to certain range for FBP and SIRT algorithms. On the other hand, distortions of the tomogram reconstructed by SART algorithms are similar for all tilting ranges. (4) Both SIRT and SART utilize iterative methods to minimize the average errors of the reconstructed volumes, but the accuracy of SIRT algorithm are worse than the SART algorithm for this dataset.

(a)

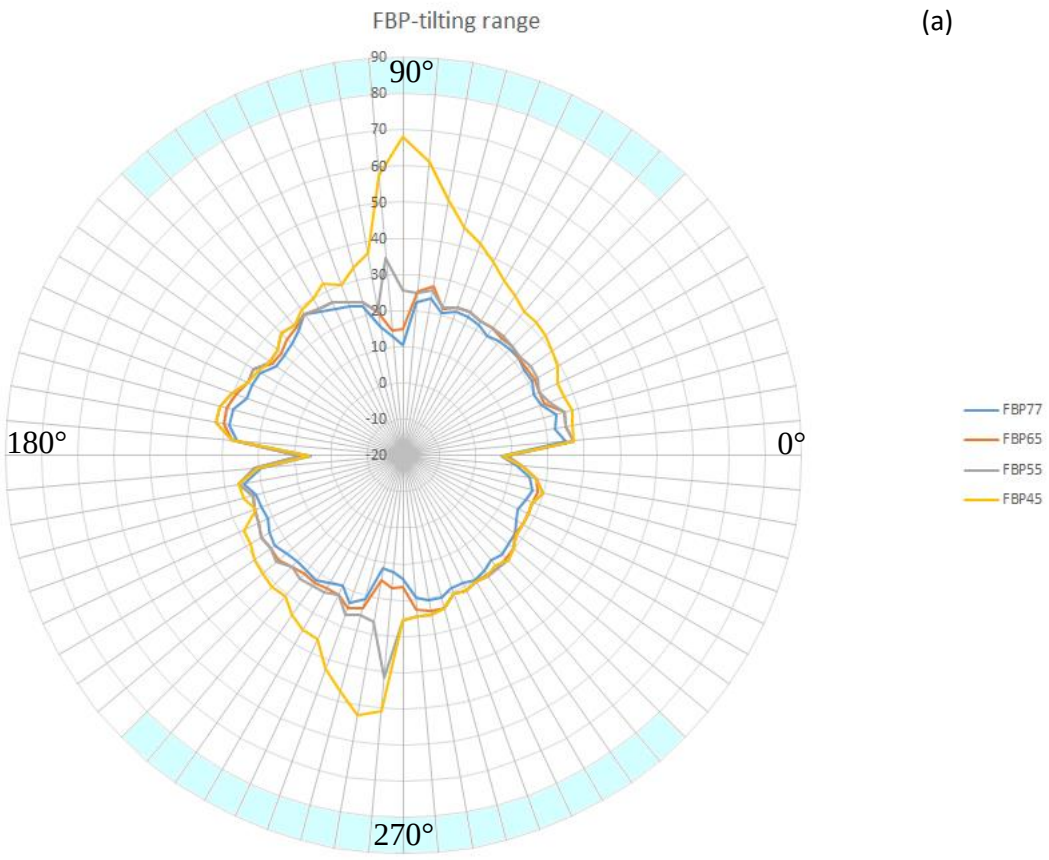
FBP-tilting range
90°
180°
0°
270°
90
80
70
60
50
40
30
20
10
0
-10
-20
FBP77
FBP65
FBP55
FBP45

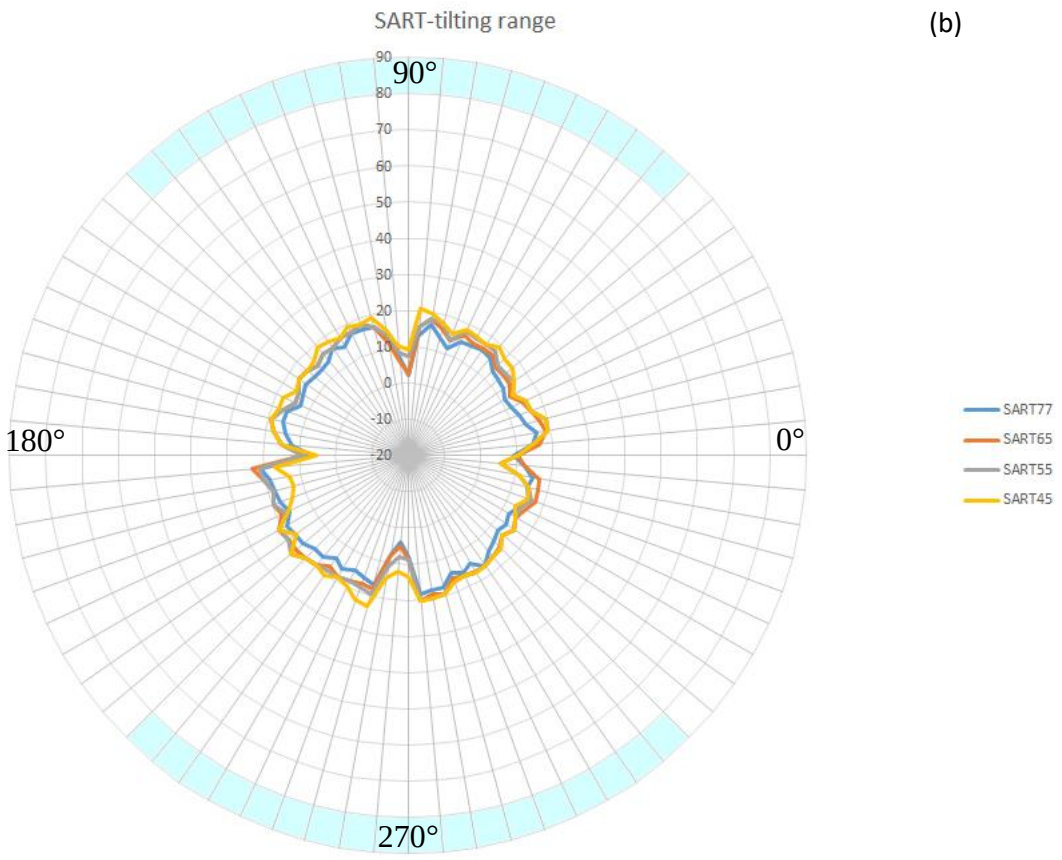
SART-tilting range
(b)
90°
80
70
60
50
40
30
20
10
0
-10
-20
180°
0°
270°
SART77
SART65
SART55
SART45

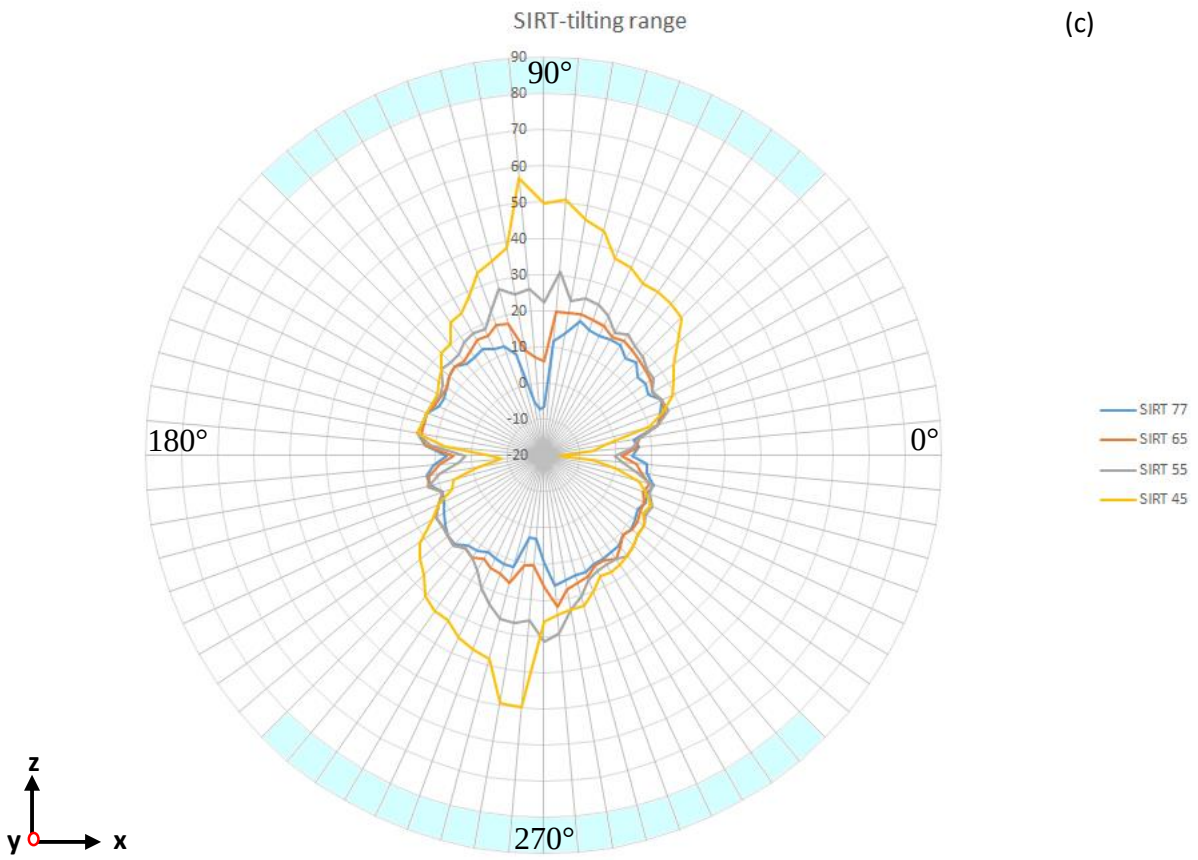

Figure 3.1. distortion of tomograms reconstructed by (a) FBP (b) SART (c) SIRT algorithm at different tilting range

Distortions of tomograms reconstructed under various increments

The distribution of the distortions remains the same regardless of the change in increment for all three tomographic algorithms, therefore the shape of reconstructed volumes remains the same. For all reconstruction algorithms, the shape of the reconstructed volume remains the same despite the change in increment (Figure 3.2).

(a)

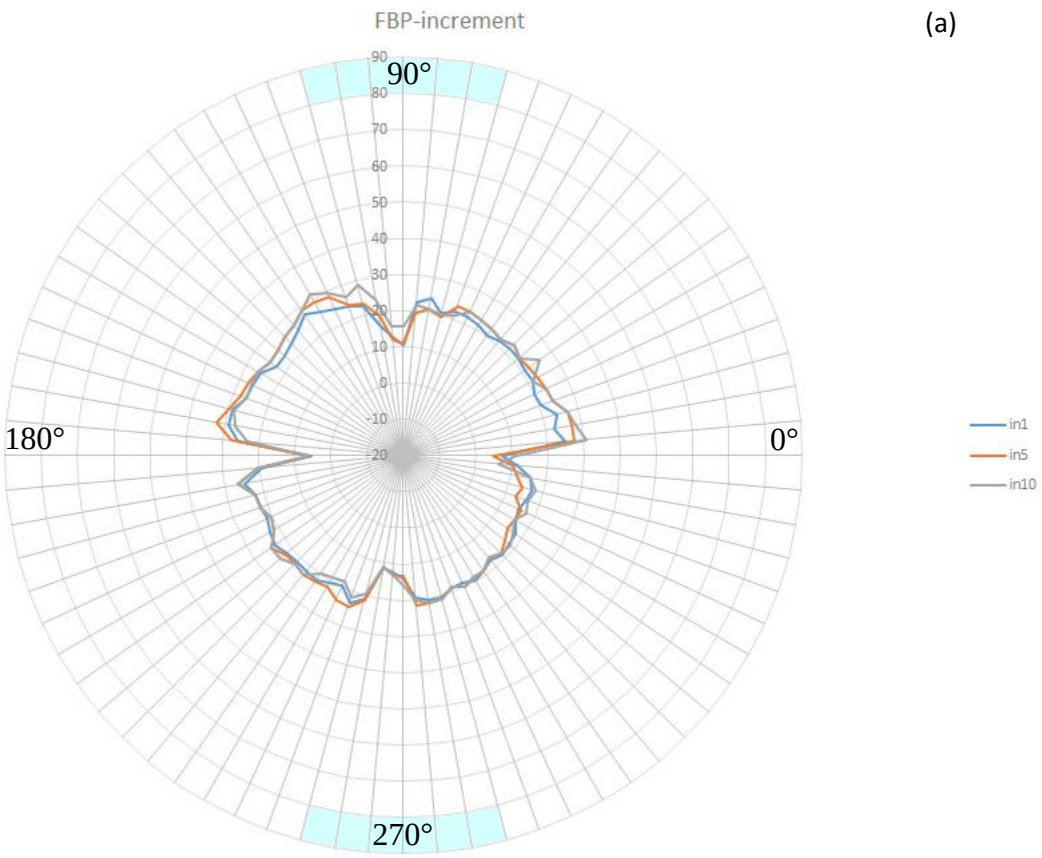
FBP-increment
90°
180°
0°
270°
90
80
70
60
50
40
30
20
10
0
-10
-20
in1
in5
in10

(b)

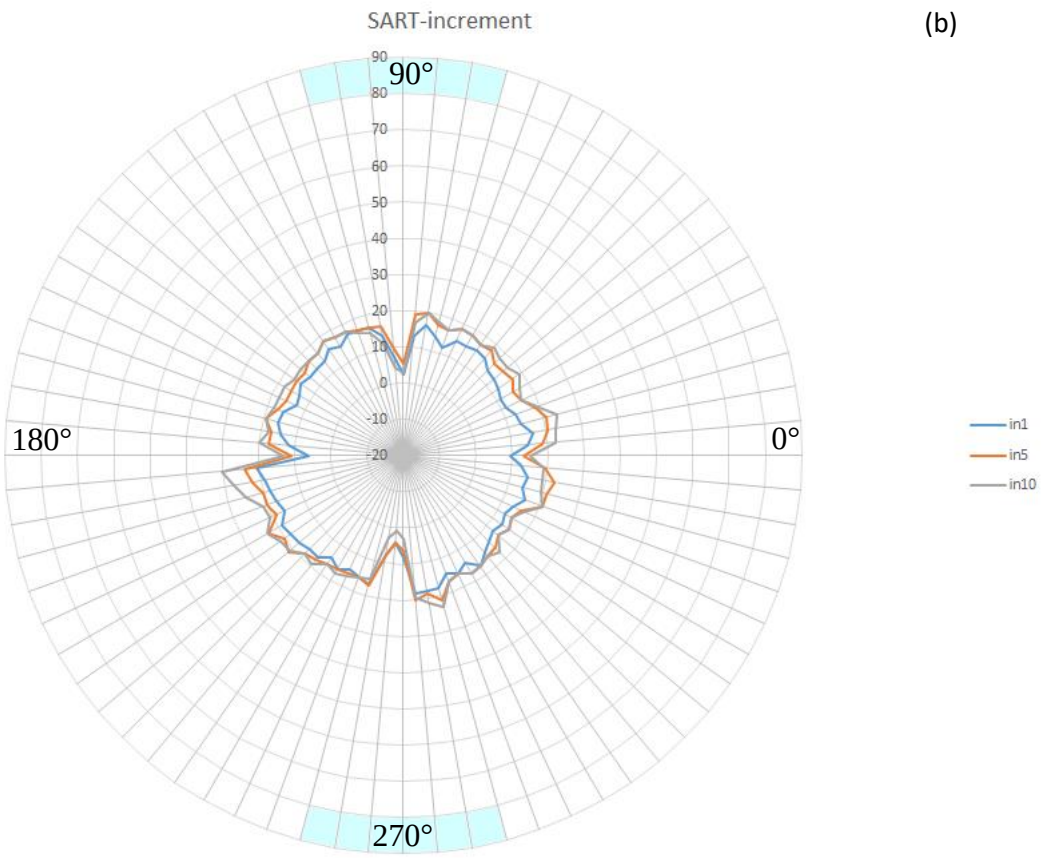
SART-increment
90°
180°
0°
270°
90
80
70
60
50
40
30
20
10
0
-10
-20
in1
in5
in10

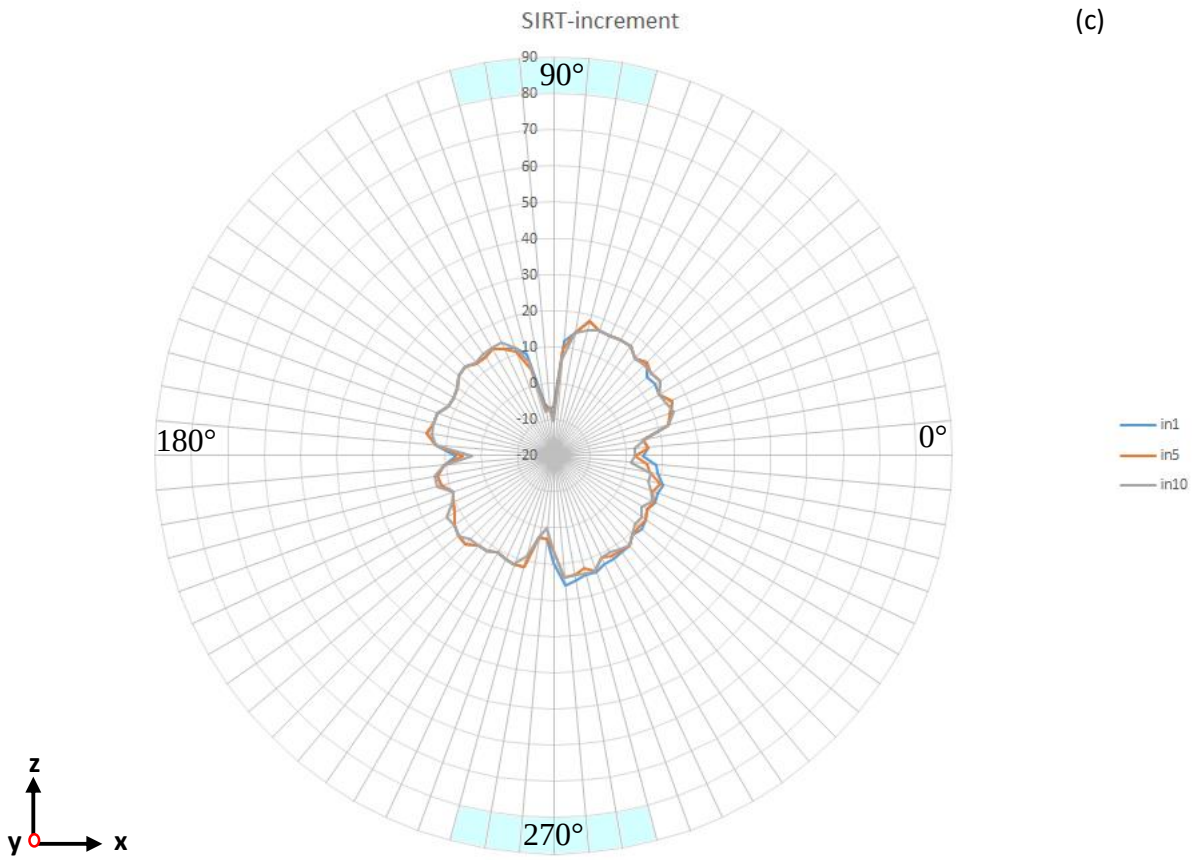

Figure 3.2. distortion of tomograms reconstructed by (a) FBP (b) SART (c) SIRT algorithm at different increment

Key observations from MgO tomograms

Two observations from Table 3.1 and Figure 3.1 contradict the general sense about distortions, i.e. distortions are expected to be the largest in the missing wedge region. First, distortions appear in all directions at high tilting range, and start to become severe, specifically in missing wedge region, as the tilting range decreases. From Saghi's study, 3D reconstructions generated from datasets with a full tilting range and small increment exhibit isotropic error, but an anisotropic degradation induced by missing wedge can be observed. Based on the results shown in Figure 3.1, reconstructed volumes were able to retain an isotropic resolution with tilting range decreased to ±65° for FBP and SIRT algorithms, and can be as low as ±45° for SART algorithm. Second, cusps in Figure 3.1 are found within the missing wedge region at high tilting range. Cusps are found at 0° and 180° because threshold was set to the value at which the tomograms match the 2D STEM image (xy plane), in consequence, the distortion is expected to be minimal in the x direction. Cusps occurred at 90° and 270° differ the common logic, i.e. the distortion should be most noticeable in the missing wedge direction; causes of the cusps could be the symmetry of the reconstructed object, which require further study to confirm. Moreover, Table 3.2 and Figure 3.2

show that the shape of the reconstructed volume remains the same despite the change in increment for all tomographic algorithms. Tilt-series with large increment provides fewer data points for the reconstruction process; it not only results in an increase of streaking artifacts and noise, but also gives weaker intensities to the tomograms. However, the shape of the tomogram can remain the same, meaning that the distortions of the reconstructed volume are mainly caused by the absent information located in the missing wedge region.

Back-projection tomographic algorithm is found to be more sensitive to tilting range compared to iterative reconstruction technique. For FBP technique, the reconstructed volume is generated by assembling the projection images taken at different view; the structural information absent from the missing wedge region cannot be restored, causing an increased in distortions and artifacts to the tomogram as the tilting range decreases. Conversely, missing wedge has a smaller impact on the iterative reconstruction technique because the average error of the tomogram is adjusted by comparing the projections of the current reconstructed volume to the original STEM projection images in each iteration step. Results from Figure 3.1 show the degree of distortion in a descending order of: FBP>SIRT> SART as the tilting range decreases. Both SIRT and SART utilize iterative methods to minimize the average errors of the reconstructed volumes, but the accuracy of SIRT algorithm is worse than the SART algorithm for this dataset. Possible reasons could be the number of iteration required for the SIRT calculation to converge is much larger than the setup, resulting in a less accurate tomogram.

Chapter 4

Case Study

Case study: Electron tomography for iron oxide

Superparamagnetic iron oxide nanoparticles with controlled size and proper surface chemistry have potential applications in magnetic resonance imaging contrast enhancement, cellular labelling/cell separation, tissue repair and drug delivery. Studies have been carried out to synthesize iron oxide nanoparticles comprise properties of high magnetic saturation, biocompatibility, monosized in the range smaller than 100 nm, interactive functions at the surface and most importantly superparamagnetic properties that do not retain any magnetism after removal of magnetic field.

Integrating imaging agents and therapeutics into one system has become prevalent in biomedical, especially for the delivery and monitoring of highly toxic compounds in vivo. Image contrast of MRI are contributed by three factors, proton density, longitudinal relaxation time (T_1) and transverse relaxation time (T_2). For T_2-weighted MRI, the sensitivity of the contrast agent is expressed in terms of the transverse relaxivity, i.e. the proton relaxation rate enhancement per millimolar of nanoparticles. The higher the transverse relaxivity, the better image contrast of T_2-weighted MRI. Magnetic iron oxide nanoparticles have been used as T_2 contrast agent because the high magnetic susceptibility of iron oxide nanoparticles can induce strong local field inhomogeneity upon exposure to an external magnetic field, leading to an increase in the NMR transverse relaxation rate of the water protons and a decrease in transverse relaxation time. The size distribution of iron oxide nanoparticles is essential because the contrast factor, transverse relaxivity, is a function of particle size, magnetization, and aggregation. Therefore, reliable characterization of the particle size distributions is important to achieve quantitative correlations of transverse relaxivities. Carroll et al[15]. have successfully predicted the transverse relaxivities of predominantly single maghemite nanoparticle; however, the accurate prediction of transverse relaxivities of magnetic nanoparticle clusters has remained a challenge because the average

particle sizes measured by dynamic light scattering show great inaccuracies. The ability to quantitatively measure the aggregated magnetic nanoparticles is needed. In this case study, 3D reconstruction of magnetic particles comprised of clusters of iron oxide nanoparticles stabilized by a biocompatible, amphiphilic diblock copolymer, poly(ethylene oxide-b-D,L-lactide) was demonstrated.[14-16]

Tomograms shown in Table 4.1-1 reveals the size of the iron oxide cluster without the induce of projection effect. For this dataset, tilt-series was collected in ±75° tilting range with 5° increment; the alignment was done by cross-correlation method without fiducial markers therefore only the lateral shift was determined. Based on the results shown in Figure 3.1 and Figure 3.2, reconstructed volumes were able to retain an isotropic resolution with tilting range decreased to ±65° for FBP and SIRT algorithms, and can be as low as ±45° for SART algorithm. Though ±75° tilting range was achieved for the tilt-series of iron oxide cluster, distortions in z direction were observed, which is especially severe for SART and SIRT algorithms. The reason of having distortions in high tilting range can be the alignment errors. For iterative methods, the average error of the tomogram is adjusted by comparing the projections of the current reconstructed volume to the original projection images in each iteration step; misalignment can cause the minimum average errors propagate in different directions. FBP-tomogram of iron oxide cluster shows less distortions in z direction, meaning that alignment errors have a smaller impact on the FBP reconstruction technique.

Table 4.1-1: tomograms of iron oxide cluster reconstructed using various algorithms

	xy plane	xz plane	yz plane
FBP	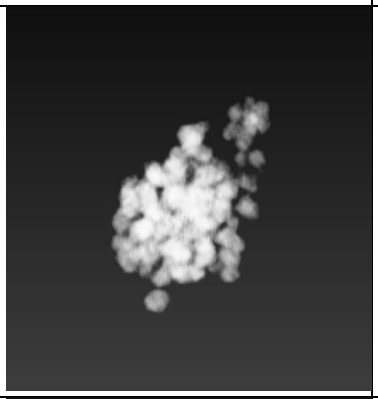		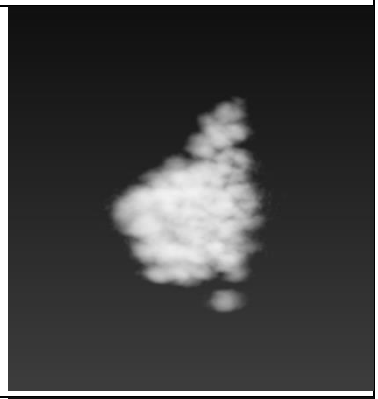
SART	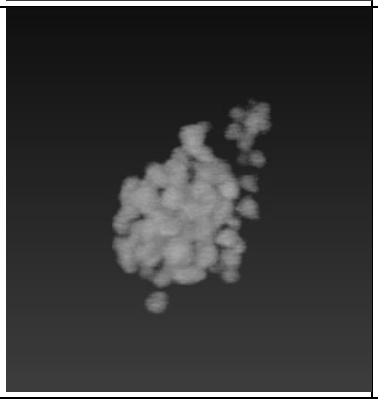	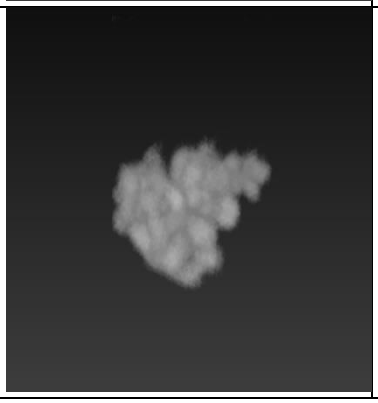	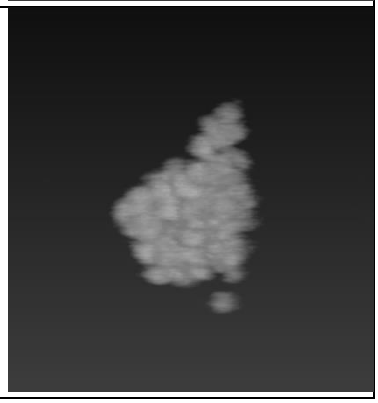

SIRT	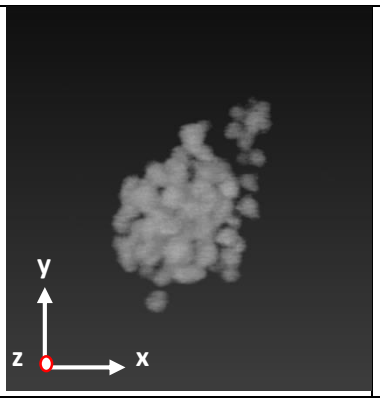	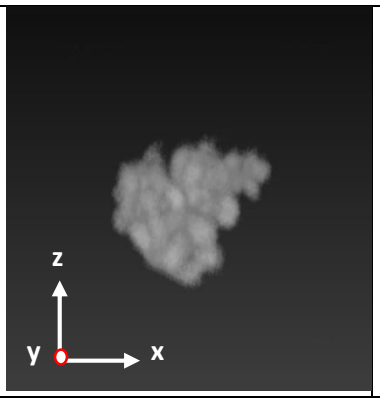	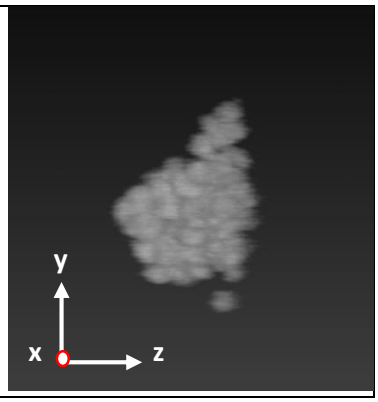

Case study: Electron tomography for PS-b-PDMS

Plastic-based materials have been widely used in daily life. With the profound development in polymerization, synthetic polymers can be produced inexpensively with the physically properties accurately controlled. To predict the properties of polymers, until recently, the majority of microscopy datasets have provided only 2D projected images. However, with the increasing complexity of polymers, the interpretation provided by the 2D data is limited. To overcome the restrictions and obtain statistical relevant information, experimental development on multi-scale (from few nm to few 100 nm) and multi-dimension electron microscopy technique were pursued; 3D electron tomography technique at the nanoscale was utilized to understand 3D structural, chemical and morphological characteristics of polymer based nanocomposits.

The lamellar structure of PS-b-PDMS block copolymer was examined using both 2D images and 3D reconstruction. Due to the viewing orientation of camera and overlap image projection caused by the complex structure of the specimen, the thickness obtained from the 2D image deviates from the 3D reconstruction, meaning that 2D image cannot fully represent real spacing of the 3D object. With further analysis of the 3D reconstruction, the distribution of lamellar structure, chemical composition and the volume of region of interest, providing us information to estimate the chemical and physical properties of the specimen can be obtained.

Thickness of Lamellar Structure in 2D and 3D

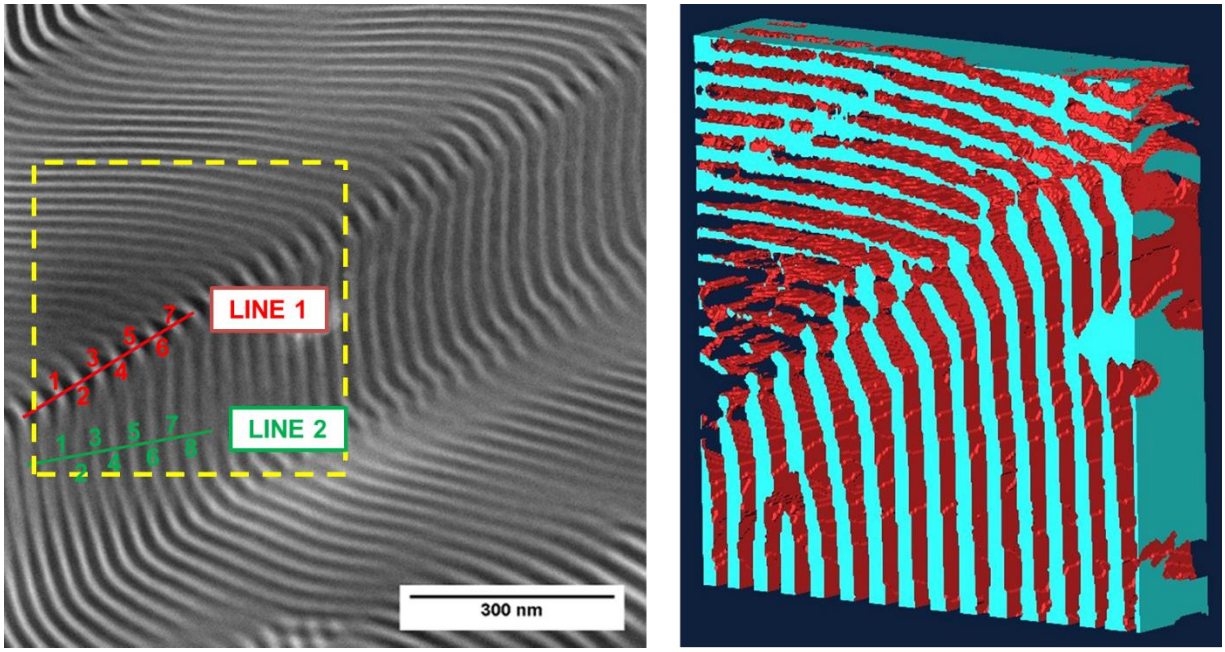

Figure 4.2-1: Lamellar structure of PS-b-PDMS ((Mn_PS=22,000, Mn_PDMS=21,000, Mw/Mn=1.08) block copolymer in (a) 2D image and (b) 3D reconstruction at the highlighted region tilted from -65° to 65° by 5° increment

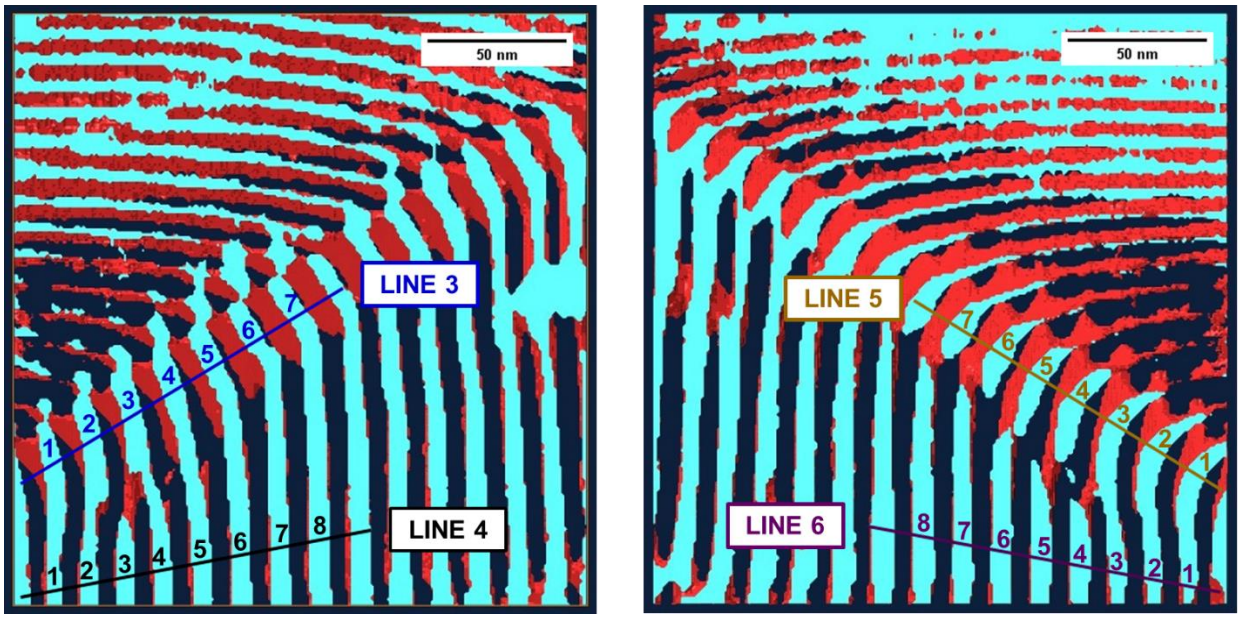

Figure 4.2-2: 3D reconstruction of y-z plane (front and rear plane)

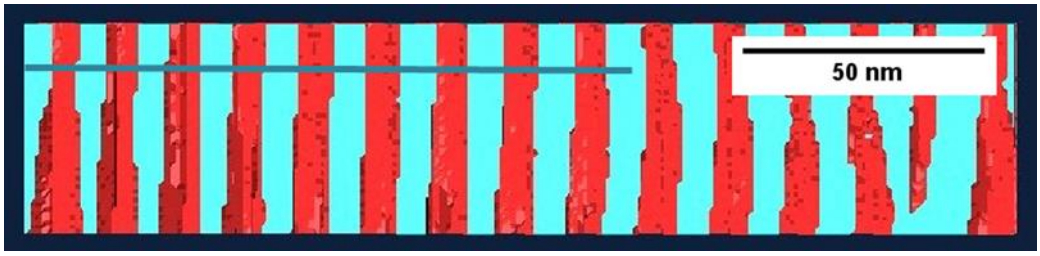

Figure 4.2-3: 3D reconstruction of x-z plane. Some lamellar structures bent at x-z plane, such morphology cannot be observed in 2D images

Table 4.2-1: Thickness of the lamellar structure (nm)

Point	Line1	Line2	Line3	Line4	Line5	Line6	Line7
1	13	10	8	6	7	5	6
2	14	15	8	7	9	7	6
3	14	12	6	6	8	7	7
4	14	10	7	7	8	8	7
5	14	15	8	7	8	9	7
6	13	13	7	7	9	7	7
7	14	15	7	7	10	7	9
8	/	15	/	8	/	8	8

Case study: Electron tomography for block copolymer thermoplastic elastomers

In the past few years, industrial applications of block copolymer thermoplastic elastomers have rapidly increased, which include hot melt adhesives, synthetic rubbery products, automobile parts, etc. The hard phase and soft phase of the block copolymers enhance the mechanical integrity and flexibility of the material, respectively. Such phase separation is crucial for thermoplastic properties and elasticity.

Relationships between thermomechanical properties and surface morphology of copolymer films have been studied. Two samples, [a] solution-cast ABA triblock copolymers with adenine acrylic (AdA) external blocks and a poly(n-butyl acrylate) (PnBA) central block and [b] solution-cast supramolecular blend of adenine/thymine-functionalized ABA triblock copolymers, have been compared in the study. Both samples have similar 2D information, such as AFM images (Figure 4.3-1) and regular TEM images (Figure 4.3-2). However, from the dynamic mechanical analysis, the latter has longer plateau window over a wider temperature range (Figure 4.3-3).[17] In order to reveal the true structure-property relationship, electron tomography technique is applied to investigate the structure of both samples in three-dimension.

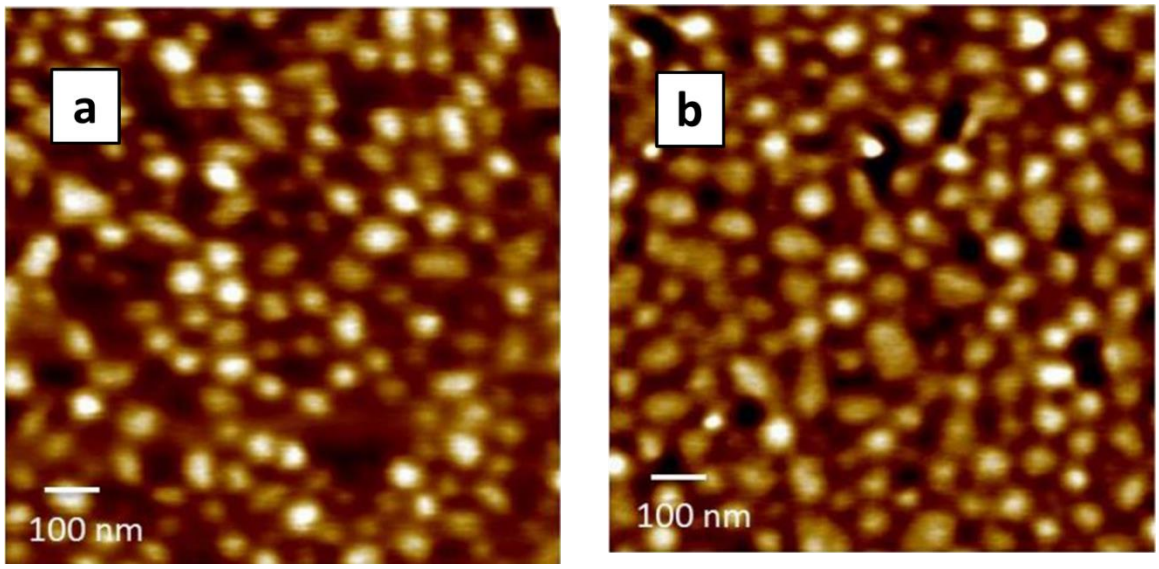

Figure 4.3-1: Tapping mode AFM phase image of (a) solution-cast Poly(AdA-b-nBA-b-AdA) and (b) supramolecular blend. The phase regions of both samples are similar in shape and size[17]

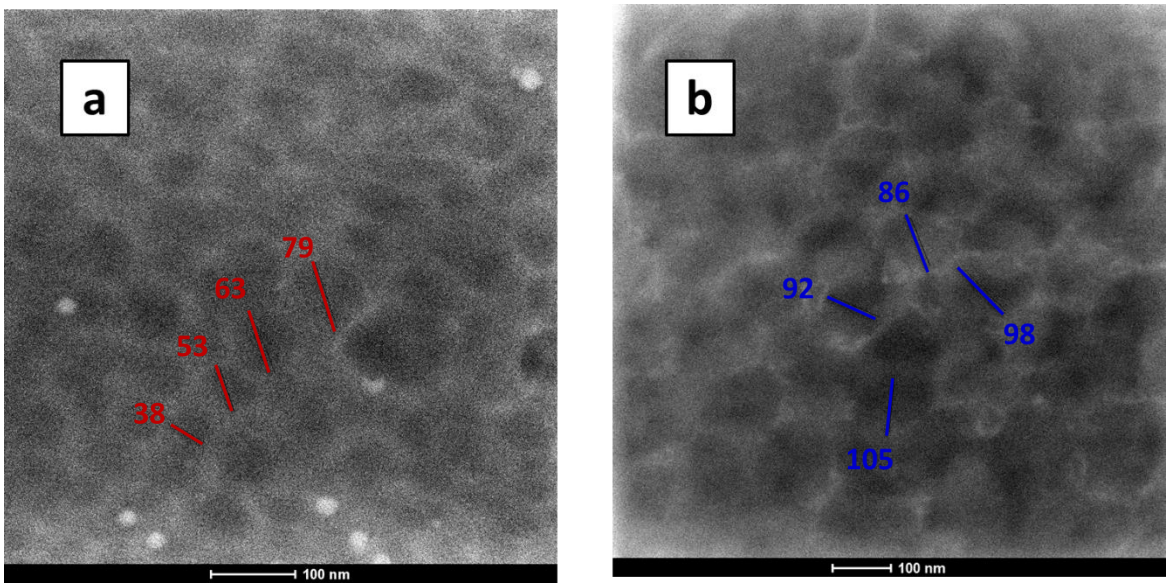

Figure 4.3-2: 2D-TEM image of (a) solution-cast Poly(AdA-b-nBA-b-AdA) and (b) supramolecular blend. Supramolecular blend has relatively uniform phase size distributed throughout the region, providing better thermomechanical properties

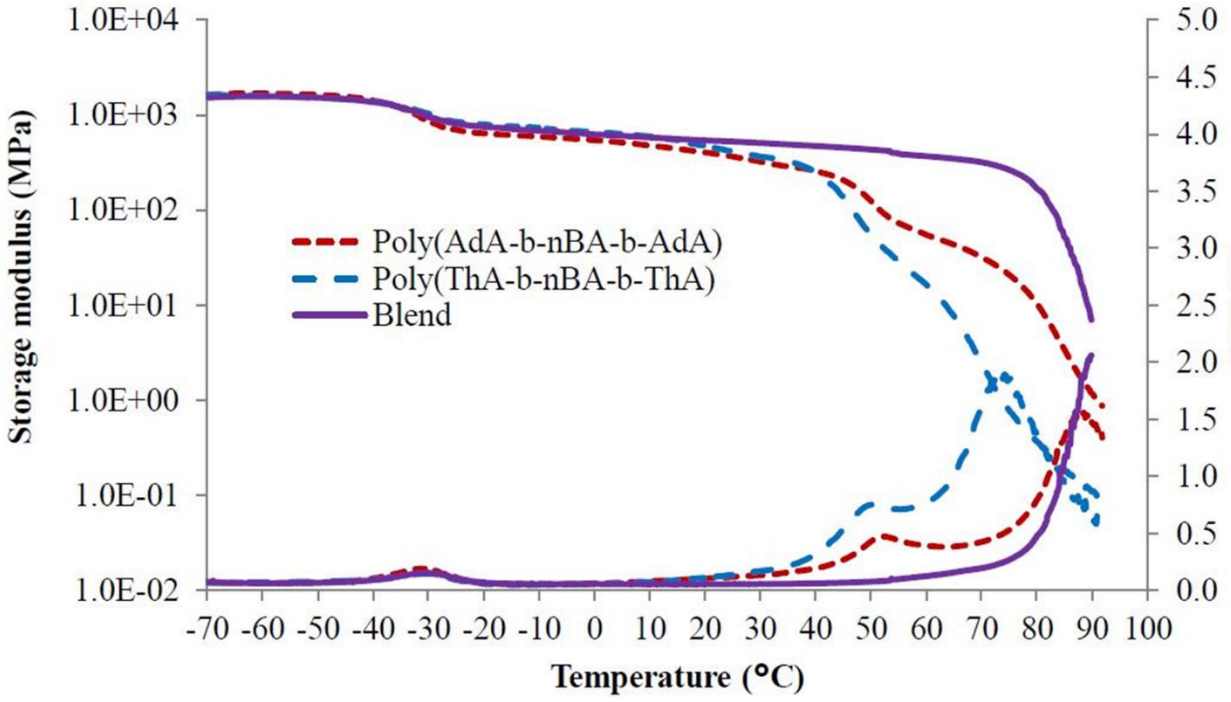

Figure 4.3-3: Effect of processing conditions on thermomechanical properties. Supramolecular blend shows approximately 40°C wider plateau window compared to the individual components[17]

3D Analysis

From the 2D-TEM images of both samples (Figure 4.3-2), we assume the phase regions are either spherical or cylindrical shape. The length of the phases in Z-direction accidentally exceeds the thickness of TEM thin foil prepared by cryo-ultra microtome. As a result, the morphology of the phases in Z-direction are not fully revealed in 3D reconstruction (Figure 4.3-4, 4.3-5). To improve the image contrast, samples were stained with Ruthenium tetroxide. Therefore, reconstructed images show better contrast at both the top and bottom surfaces, while the contrast is lower in the interior. Based on 3D-TEM, the morphology of phases in the solution-cast sample appears to be spherical, whereas that of supramolecular sample is not conclusive because of the TEM foil thickness issue (Figure 4.3-6).

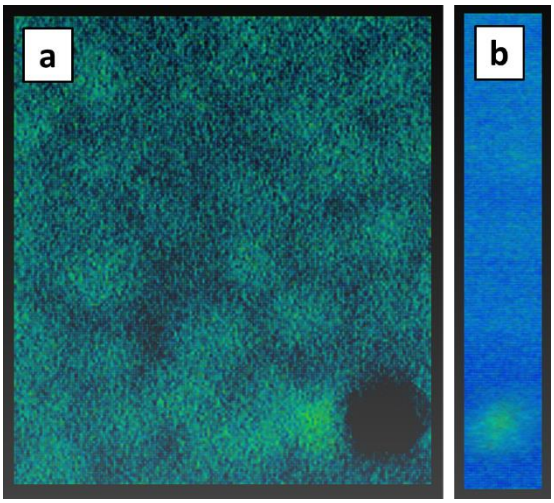

Figure 4.3-4: 3D reconstruction of Poly(AdA-b-nBA-b-AdA) in (a) x-y plane and (b) x-z plane

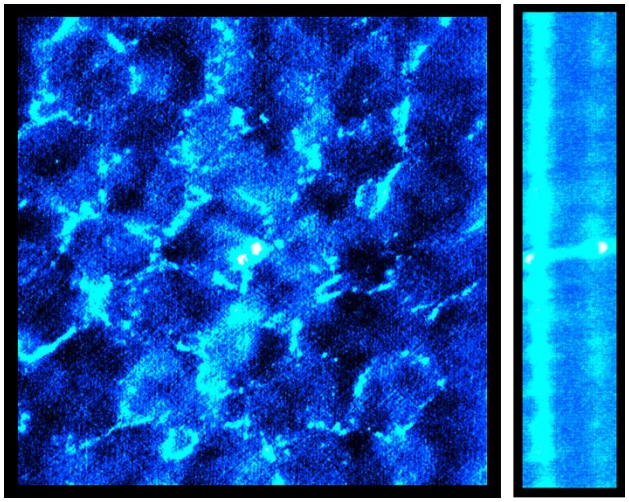

Figure 4.3-5: 3D reconstruction of supramolecular blend in (a) x-y plane and (b) x-z plane

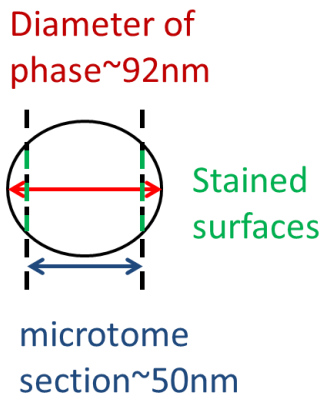

Figure 4.3-6: cross-sectional view of TEM thin foil prepared by cryo-ultra microtome

Chapter 5

Conclusion

From the MgO reconstruction results, distortions appear in all directions at high tilting range; an isotropic resolution can be retained with tilting range decreased to ±65° for FBP and SIRT algorithms, and can be as low as ±45° for SART algorithm. Distortions become severe, specifically in missing wedge region, as the tilting range continues to decrease. Cusps are found in the missing wedge region at high tilting range, which could be caused by the symmetry of the reconstructed object; further study is required to confirm this speculation. The degree of distortion in a descending order is: FBP>SIRT> SART as the tilting range decreases, indicating that FBP is most influenced by the tilting range whereas SART is least influenced by the tilting range. The distribution of the distortions remains the same regardless of the change in increment for FBP, SART and SIRT tomographic algorithms, therefore the shape of reconstructed volumes remains the same despite the change in increment.

References

1. Monsegue, N.; Reynolds, W. T.; Hawk, J. A.; Murayama, M., How TEM Projection Artifacts Distort Microstructure Measurements: A Case Study in a 9 pct Cr-Mo-V Steel. *Metallurgical and Materials Transactions a-Physical Metallurgy and Materials Science* **2014,** *45A* (9), 3708-3713.

2. Tessonnier, J. P.; Ersen, O.; Weinberg, G.; Pham-Huu, C.; Su, D. S.; Schlogl, R., Selective Deposition of Metal Nanoparticles Inside or Outside Multiwalled Carbon Nanotubes. *Acs Nano* **2009,** *3* (8), 2081-2089.

3. Zecevic, J.; Gommes, C. J.; Friedrich, H.; de Jongh, P. E.; de Jong, K. P., Mesoporosity of Zeolite Y: Quantitative Three-Dimensional Study by Image Analysis of Electron Tomograms. *Angewandte Chemie-International Edition* **2012,** *51* (17), 4213-4217.

4. Jinnai, H.; Spontal, R. J., Transmission electron microtomography in polymer research. *Polymer* **2009,** *50* (5), 1067-1087.

5. Fernandez, J. J., Computational methods for materials characterization by electron tomography. *Current Opinion in Solid State & Materials Science* **2013,** *17* (3), 93-106.

6. Jinnai, H.; Spontak, R. J.; Nishi, T., Transmission Electron Microtomography and Polymer Nanostructures. *Macromolecules* **2010,** *43* (4), 1675-1688.

7. Sugimori, H.; Nishi, T.; Jinnai, H., Dual-axis electron tomography for three-dimensional observations of polymeric nanostructures. *Macromolecules* **2005,** *38* (24), 10226-10233.

8. Kawase, N.; Kato, M.; Nishioka, H.; Jinnai, H., Transmission electron microtomography without the "missing wedge" for quantitative structural analysis. *Ultramicroscopy* **2007,** *107* (1), 8-15.

9. Midgley, P. A.; Weyland, M., STEM Tomography. In *Scanning Transmission Electron Microscopy: Imaging and Analysis*, Pennycook, J. S.; Nellist, D. P., Eds. Springer New York: New York, NY, 2011; pp 353-392.

10. Midgley, P. A.; Weyland, M., 3D electron microscopy in the physical sciences: the development of Z-contrast and EFTEM tomography. *Ultramicroscopy* **2003,** *96* (3-4), 413-431.

11. Frank, J., *Electron tomography: methods for three-dimensional visualization of structures in the cell*. Springer: New York, 2006.

12. Leary, R.; Saghi, Z.; Midgley, P. A.; Holland, D. J., Compressed sensing electron tomography. *Ultramicroscopy* **2013,** *131*, 70-91.

13. Saghi, Z.; Divitini, G.; Winter, B.; Leary, R.; Spiecker, E.; Ducati, C.; Midgley, P. A., Compressed sensing electron tomography of needle-shaped biological specimens - Potential for improved reconstruction fidelity with reduced dose. *Ultramicroscopy* **2016,** *160*, 230-238.

14. Balasubramaniam, S.; Kayandan, S.; Lin, Y. N.; Kelly, D. F.; House, M. J.; Woodward, R. C.; St Pierre, T. G.; Riffle, J. S.; Davis, R. M., Toward Design of Magnetic Nanoparticle Clusters Stabilized by Biocompatible Diblock Copolymers for T-2-Weighted MRI Contrast. *Langmuir* **2014,** *30* (6), 1580-1587.

15. Carroll, M. R. J.; Woodward, R. C.; House, M. J.; Teoh, W. Y.; Amal, R.; Hanley, T. L.; St Pierre, T. G., Experimental validation of proton transverse relaxivity models for superparamagnetic nanoparticle MRI contrast agents. *Nanotechnology* **2010,** *21* (3).

16. Laurent, S.; Forge, D.; Port, M.; Roch, A.; Robic, C.; Elst, L. V.; Muller, R. N., Magnetic iron oxide nanoparticles: Synthesis, stabilization, vectorization, physicochemical characterizations, and biological applications. *Chemical Reviews* **2008,** *108* (6), 2064-2110.

17. Zhang, K. T., S.J., Influence of Adenine and Thymine Binding Ratio on ABC Triblock Copolymer Self-Assembly. *Royal Society of Chemistry*.